Observations of fog-aerosol interactions over central Greenland

Heather Guy[1,2], Ian M. Brooks[2], David D. Turner[3], Christopher J. Cox[4], Penny M. Rowe[5], Matthew D. Shupe[6,4], Von P. Walden[7], Ryan R. Neely III[1,2]

[1]National Centre for Atmospheric Science, Leeds, U.K.
[2]School of Earth and Environment, University of Leeds, U.K.
[3]3Global Systems Laboratory, National Oceanic and Atmospheric Administration, Boulder, CO, USA
[4]Physical Sciences Laboratory, National Oceanic and Atmospheric Administration, Boulder, USA
[5]NorthWest Research Associates, Redmond, WA, USA
[6]University of Colorado, Cooperative Institute for Research in Environmental Sciences, Boulder, USA
[7]Department of Civil and Environmental Engineering, Laboratory for Atmospheric Research, Washington State University, Pullman, WA, USA

Key Points:

- Ground-based measurements of downwelling longwave radiation can be used to determine the microphysical properties of optically thin fogs.
- Almost all aerosol particles larger than 250 nm diameter are scavenged during twelve summer fog events in central Greenland.
- Multiple pathways exist through which the aerosol population can impact fog development, and fog can modify the surface aerosol population.

Corresponding author: Heather Guy, `heather.guy@ncas.ac.uk`

Abstract

Supercooled fogs can have an important radiative impact at the surface of the Greenland Ice Sheet, but they are difficult to detect and our understanding of the factors that control their lifetime and radiative properties is limited by a lack of observations. This study demonstrates that spectrally resolved measurements of downwelling longwave radiation can be used to generate retrievals of fog microphysical properties (phase and particle effective radius) when the fog visible optical depth is greater than ∼0.25. For twelve cases of fog under otherwise clear skies between June and September 2019 at Summit Station in central Greenland, nine cases were mixed-phase. The mean ice particle (optically-equivalent sphere) effective radius was 24.0 ± 7.8 μm, and the mean liquid droplet effective radius was 14.0 ± 2.7 μm. These results, combined with measurements of aerosol particle number concentrations, provide observational evidence supporting the hypotheses that (a) low surface aerosol particle number concentrations can limit fog liquid water path, (b) fog can act to increase near-surface aerosol particle number concentrations through enhanced mixing, and (c) multiple fog events in quiescent periods gradually deplete near-surface aerosol particle number concentrations.

Plain Language Summary

Fogs over the central Greenland Ice Sheet can modify the net radiation that reaches the ice surface. How much a fog influences the net surface radiation is related to the fog lifetime and optical depth. These properties are related to the phase and size distribution of the particles that make up the fog, that in turn depend on the characteristics of the atmospheric aerosol particles on which the fog forms. This study shows that the phase and size distribution of fog particles can be determined from ground-based measurements of downwelling longwave radiation, and explores how fogs interact with the number concentration of atmospheric aerosols measured near the surface during twelve cases of summertime fog in central Greenland.

1 Introduction

Central Greenland is a unique environment in the Northern Hemisphere: A uniform surface of snow-covered ice extends for over 250 km in every direction from the ice sheet's highest point at 3,250 m a.s.l (Howat et al., 2017). The structure of the atmospheric boundary layer over the ice sheet is driven by large-scale circulation, including atmospheric rivers associated with extratropical storms (Mattingly et al., 2018; Gallagher et al., 2018) and blocking anticyclones (Pettersen et al., 2022), and is modulated locally by strong radiative cooling at the ice sheet surface (Hoch et al., 2007). Under quiescent conditions (clear skies, light winds), surface radiative cooling frequently drives the formation of supercooled radiation fog through the condensation of water onto aerosol particles that act as cloud condensation nuclei (CCN) (Bergin et al., 1994; Cox et al., 2019).

At Summit Station (Summit), a research base located at the highest point on the Greenland Ice Sheet (72.57°N, -38.47°E), fogs comprised of supercooled droplets occur year-round even when the surface temperature falls below -30°C (Cox et al., 2019). These fogs can have a strong effect on the ice sheet surface energy budget, contributing on average an additional 27 W m^{-2} of total net downwelling radiation relative to clear sky conditions (Cox et al., 2019). In the summer months (May to September) solar heating of the ice sheet surface during the day results in a diurnal cycle of net surface radiation. Radiation fog forms during the period of the diurnal cycle when the sun elevation is lowest and the net radiative cooling at the surface is strongest, and the associated increase in net downwelling longwave radiation acts to damp the diurnal temperature cycle, which has been hypothesised to precondition the ice sheet surface for melt (Cox et al., 2019). These fogs can also increase the rate of aerosol deposition to the surface (Bergin et al.,

1994, 1995) and reduce ice sheet mass loss by recondensing sublimated water onto fog particles that then settle out under gravity (Berkelhammer et al., 2016).

Understanding the controls on the processes that modify the surface mass balance of the Greenland Ice Sheet is becoming increasingly important as melt events become more common and widespread (Tedesco & Fettweis, 2020; Hanna et al., 2021). The radiative impact of fog at the ice sheet surface depends on fog occurrence, duration, and optical depth, which itself is determined by the fog liquid water path (LWP), and microphysical properties such as fog particle phase and size distribution. The representation of fog microphysical properties is one of the largest sources of uncertainty in fog forecast models and Large-eddy simulations (Boutle et al., 2022), and the representation of cloud microphysical properties in general is one of the largest sources of uncertainty in projections of future Greenland Ice Sheet melt (Hofer et al., 2019). One of the reasons for these uncertainties is that there are very limited observations available to constrain model parameterisations. This is particularly true for fog over Greenland, which often occurs in shallow layers (< 100 m) below the lowest range gate of most ground-based active remote sensing instruments (such as radar or lidar). These very shallow fog layers are often subgrid-scale for most climate and weather models.

Important controls on fog (and cloud) lifetime, microphysical, and radiative properties are the number concentration, size distribution, and composition of aerosol particles on which droplets or ice crystals can form. Droplets form on CCN, so the number concentration of CCN determines the number concentration of droplets at a given supersaturation. When the CCN concentration is increased, a fog will contain a greater number of smaller droplets than an equivalent fog (with the same liquid water content) forming under a reduced CCN concentration, resulting in a relatively high fog optical depth and solar reflectivity, and hence impacting the net downwelling radiation at the surface (Twomey, 1977). Increased fog droplet number concentration also leads to enhanced longwave radiative cooling at fog top (e.g. Garrett, Radke, & Hobbs, 2002), encouraging further droplet activation, and smaller droplets that are not removed as quickly by sedimentation, with both processes working to extend fog lifetime (Maalick et al., 2016; Boutle et al., 2018; Yan et al., 2021). Increased fog top cooling can also enhance mixing and entrainment that, depending on the humidity of the overlying air, can either reduce or increase cloud/fog water content (Ackerman et al., 2004; Small et al., 2009; Williams & Igel, 2021).

In very clean environments, low CCN concentrations can limit fog (and cloud) formation and lifetime, because the few activated CCN will grow to relatively large sizes and precipitate out, removing CCN and preventing further droplet formation (Mauritsen et al., 2011; Stevens et al., 2018). Evidence suggests that this situation can occur in the Arctic, where naturally low concentrations of CCN (1 to 100 cm^{-3}) have the potential to control cloud radiative properties (Mauritsen et al., 2011; Sterzinger et al., 2022). At Summit, the annual mean aerosol particle concentration is low even compared to other Arctic sites (Schmeisser et al., 2018); the mean annual total surface aerosol particle number concentration (> 20 nm) at Summit in 2019-2020 was just 129 cm^{-3}, and fell to less than 10 cm^{-3} on occasions in all seasons (Guy et al., 2021). Given that only some of these aerosol particles act as CCN, these numbers are an upper limit on the number of CCN available near the surface where fog forms.

When the temperature is below freezing, which is the case almost all the time in central Greenland (Shupe et al., 2013), the phase partitioning of the fog is also important for fog lifetime and the radiative effect of the fog at the surface. Ice fogs usually form through the direct deposition of vapour onto ice-nucleating particles (INPs, a subset of the aerosol population that can catalyse freezing) when the air is supersaturated with respect to ice (Gultepe et al., 2015). Ice nucleation can also occur in supercooled liquid fogs by either immersion freezing (INPs are activated within a droplet) or contact freezing (droplets freeze upon contact with an INP) (Kanji et al., 2017). Once primary ice

is present, further ice can form through several different multiplicative mechanisms, collectively known as secondary ice production (Field et al., 2017). If the air becomes supersaturated with respect to ice but subsaturated with respect to water, ice crystals will grow at the expense of liquid water droplets, causing the liquid droplets to evaporate and the ice crystals to grow to relatively large sizes and settle out, removing moisture from the surface layer and acting to reduce fog lifetime; this is known as the Wegener-Bergeron-Findeisen process (e.g. Korolev, 2007).

In addition to the aerosol population having the potential to control fog lifetime and radiatively important microphysical properties, fog formation may also be an important control on the lifecycle of aerosol particles in the boundary layer over central Greenland. Fog can act as an aerosol sink, because the fog droplet deposition flux exceeds that of aerosol dry deposition (Bergin et al., 1994, 1995). Through this mechanism, fog may act to 'clean' the boundary layer of CCN and INP, which may in turn impact fog and/or cloud formation later in time. Conversely, fog could act to increase aerosol particles in the boundary layer by enhancing the transport of aerosol particles from above the fog top into the surface layer, either by buoyancy or windshear driven turbulent entrainment at fog top, or by aerosol activation at fog top followed by droplet evaporation closer to the surface. Observational and model studies have demonstrated that the latter process can be important in low-level Arctic stratocumulus (Solomon et al., 2014; Igel et al., 2017).

The relative importance of each of these fog-aerosol interactions over central Greenland is unknown, and our ability to model these processes is hindered by a lack of observations of both fog microphysical properties and surface aerosol number concentration and size distribution. Using in-situ measurements collected at Summit in 2013-2014, Cox et al. (2019) completed a comprehensive assessment of the occurrence, microphysical characteristics, and radiative properties of fogs at Summit, but there were no aerosol particle measurements available during this period. This study builds on the findings of Cox et al. (2019), and has two main objectives: (1) to explore the possibility of using spectral measurements of downwelling longwave radiation to generate retrievals of fog microphysical properties, and (2) to use these results alongside measurements of surface aerosol particle number concentration to look for observational evidence of fog-aerosol interactions over central Greenland.

The spectral signature of downwelling longwave radiation is sensitive to the radiative properties of fog that are important for the ice sheet surface energy budget and can be measured continuously by passive ground-based instrumentation that, unlike many active remote sensing instruments, are not limited by the height of their lowest range gate and so do not have a 'blind' spot close the surface. Such measurements have been used to study the microphysical properties of mixed-phase polar clouds (Mahesh et al., 2001; Rathke et al., 2002; Turner, 2005; Garrett & Zhao, 2013; Cox et al., 2014; Shupe et al., 2015; Lubin et al., 2020; Richter et al., 2022); however, these studies did not specifically focus on fog.

Here, we use a case-study based approach to examine the advantages and limitations of retrieving the microphysical properties of fog from downwelling longwave radiation measurements. Such measurements have the greatest sensitivity to the microphysical properties of clouds when the atmosphere is dry and the clouds are low and optically thin. In addition, retrieval accuracy relies on a well-constrained cloud temperature. Taken together, this makes such measurements ideal for studying fog over central Greenland.

For objective (2), we combine the results of the fog microphysical retrievals with measurements of surface aerosol particle number concentrations and supplementary observations of atmospheric state to look for observational evidence to support (or negate) the following hypotheses:

(a) That low aerosol particle number concentration can be a critical control on fog liquid water path and lifetime.
(b) That fogs can act to increase surface aerosol particle number concentration by enhancing mixing of air from above into near-surface stable layer.
(c) That multiple fog events during quiescent conditions act to deplete near surface aerosol particle number concentration, impacting fog development later in time.

The results of this analysis may be used as the basis of future modelling studies to systematically distinguish the importance of different fog-aerosol interaction processes, and to identify instrumentation requirements for future observational campaigns to study fog-aerosol interactions over central Greenland or in similar environments.

2 Measurements and instrumentation

We make use of measurements from the ICECAPS project (the Integrated Characterisation of Energy, Clouds, Atmospheric state, and Precipitation at Summit; Shupe et al., 2013) which consists of a suite of instrumentation for monitoring atmospheric processes at Summit. To generate the microphysical retrievals of fog properties we use data from the Atmospheric Emitted Radiance Interferometer (AERI), which measures spectrally resolved downwelling infrared radiance between 3 and 19 μm at $\sim$0.48 cm^{-1} resolution (Knuteson et al., 2004b, 2004a). At Summit, the AERI measures downwelling radiation continuously, alternating between views of the sky at zenith and two calibration sources, resulting in sky measurements every 15-20 s. The AERI data are quality controlled as described in Guy et al. (2022) and subjected to noise filtering using the technique described by Antonelli et al. (2004) and Turner et al. (2006). Section 3 describes the retrieval algorithm.

To explore individual fog cases in more depth we examine data from the ceilometer (CT25K, Münkel, 2006), sodar (Neff et al., 2008), total sky imager, and near-surface temperature profiles and sensible heat flux estimates from tower-mounted in-situ sensors (Guy et al., 2020). Data from the millimetre cloud radar and precipitation occurrence sensor system were used to help identify fog cases during the summer of 2019, and radiosonde data were used to help constrain retrievals of continuous thermodynamic profiles from the AERI that are required as an input to the microphysical retrieval algorithm; both steps are described in detail in Guy et al. (2022). See Shupe et al. (2013) for further information about the overall ICECAPS instrumentation suite.

2.1 Aerosol particle measurements

During the summer of 2019 there were two instruments at Summit measuring surface aerosol particle number concentration in different size ranges: a butanol-based condensation particle counter (CPC, GRIMM 5.400) that measured the total concentration of condensation nuclei every second, and an optical particle counter (SKYOPC, GRIMM 1.129) that measured size-resolved concentrations of 250 to 4500 nm diameter particles every six seconds. Guy et al. (2021) describe the CPC data in more detail, including the estimation of particle loss in the inlet line, which resulted in the CPC measuring the number concentration of condensation nuclei with diameters between 20 and 230 nm with greater than 50% efficiency. For this reason, measurements from the CPC are henceforth referred to as N_{20}, indicating the number concentration of particles $>$ 20 nm diameter.

The SKYOPC had an identical inlet to the CPC but a higher flow rate (1.2 L min^{-1}), and as a result larger particles could pass through the SKYOPC inlet. After accounting for particle losses in the inlet (using the Particle Loss Calculator, Von der Weiden, Drewnick, & Borrmann, 2009), the SKYOPC measured the number concentration of particles with diameters between 250 and 4500 nm with greater than 50% efficiency. For the SKYOPC, the measurements were corrected for particle loss in the inlet by multiplying

the particle number concentration by a correction factor based on the modelled inlet efficiency as a function of particle size (which varied from 1.02 to 1.97 in the 250 to 4500 nm size range). The total particle number concentration between 250 and 4500 nm (henceforth N_{250}) was calculated by summing the corrected size resolved SKYOPC data.

Particles larger than 6 μm in diameter, which is smaller than the typical size of fog droplets (e.g. Mazoyer, Burnet, & Denjean, 2022), could not pass through either inlet, and the instruments were located in a heated building that was always >15°C warmer than the outside air. Thus, during fog events, we assume that N_{20} and N_{250} are measurements of the dried interstitial aerosol particle number concentration. Both N_{20} and N_{250} were resampled to five-minute medians for the purpose of this study, and quality controlled to remove any instances of contamination from station pollution as in Guy et al. (2021). Note that this quality control does not impact any of the data presented here, because none of the fog cases coincide with local pollution events (which was part of the original event selection criteria).

Figure 1 shows how the measurements from the SKYOPC (N_{250}) and CPC (N_{20}) intersect with the 'typical' size range of CCN and INP from past literature, although the proportion of aerosol particles that can act as a CCN depends on the aerosol type and degree of supersaturation, and our knowledge of the typical size range of INP particles is limited by sparse observations (particularly of small INP particles < 250 nm diameter). Supersaturations can reach higher values when the aerosol particle number concentration is low, and particles as small as 20 nm have been observed to act as CCN in clean Arctic environments (Leaitch et al., 2016; Baccarini et al., 2020). Several studies indicate that the INP population is mostly made up of coarse-mode particles > 250 nm diameter (Mason et al., 2016; Creamean et al., 2018; Si et al., 2018), however recent studies of size-resolved INP concentration over the central Arctic suggest that particles as small as 150 nm diameter can be an important source of INP (Creamean et al., 2022; Porter et al., 2022). Figure 1 also shows how measurements during the summer of 2019 compare to those collected between 15 May and 16 June 2007 using a scanning mobility particle sizer to detect particles with diameters from 5.5 to 195 nm diameter (Ziemba et al., 2010), and how they compare to the 'typical' size distribution of near-surface aerosol particles in the Arctic summer, which is mostly based on measurements from coastal and low elevation Arctic sites (Carslaw, 2022).

2.2 Fog events

We focus on the twelve radiation fog events identified by Guy et al. (2022) that occurred during the summer of 2019 (Table 1). Each fog event occurred under otherwise clear skies and had a detectable longwave radiative impact at the surface; the duration of each fog event was defined as when the 962 cm^{-1} downwelling radiance measured by the AERI is greater than a threshold of 1.7 RU (1 RU = 1 mW m^{-2} sr^{-1} cm^{-1}), which is three standard deviations above the mean clear sky radiance between June and September 2019. The 962 cm^{-1} microwindow is almost completely transparent under clear skies for conditions at Summit, and is therefore particularly sensitive to the presence of clouds (e.g. Cox, Walden, & Rowe, 2012). Note that this radiative definition of fog is distinct from the traditional definition of fog (a reduction of horizontal visibility to < 1,000 m) but is appropriate for this study because we are concerned with the radiative impact of fog on the surface energy budget. See Guy et al. (2022) for further details about the selection criteria for each of these case studies.

Table 1 details each case study and indicates where aerosol particle number concentration measurements are available. The SKYOPC vacuum pump experienced intermittent faults resulting in missing N_{250} data for some of the fog cases, and an issue with the CPC power supply resulted in incomplete N_{20} data for case 3.

Table 1. Details of fog events and data availability. Adapted from table 3 in Guy et al. (2022) and includes the mean temperature (T) and water vapor mixing ratio (wv) during each event. The minimum visibility comes from observer reports at 00, 12 and 18 UTC and may not represent the minimum visibility outside of these times. NA indicates where no data are available. Local time is UTC-3h.

ID	Case start Date Time. UTC, 2019	Case end Date Time UTC, 2019	Duration (h)	Mean surface T (°C)	Mean surface wv (g kg^{-1})	Min. visibility observer log	Min. ceilometer vertical visibility	Particle conc. available
1	08 Jun 03:30	08 Jun 05:50	2.3	-17	1.3	NA	30 m	N_{20} only
2	12 Jun 02:55	12 Jun 10:30	7.6	-8.9	2.7	NA	30 m	N_{20} only
3	13 Jul 23:25	14 Jul 04:30	5.1	-21	0.93	1,600 m	30 m	N_{250} only
4	15 Jul 23:10	16 Jul 10:30	11	-19	1.0	400 m	30 m	Yes
5	31 Jul 23:25	01 Aug 04:35	5.2	-8.6	2.7	400 m	25 m	N_{20} only
6	01 Aug 22:00	02 Aug 14:40	17	-12	2.0	800 m	20 m	N_{20} only
7	04 Aug 06:35	04 Aug 08:15	1.7	-17	1.2	NA	NA	Yes
8	04 Aug 22:40	05 Aug 11:50	13	-18	1.2	400 m	15 m	Yes
9	06 Aug 01:05	06 Aug 10:00	8.9	-21	0.82	NA	30 m	N_{20} only
10	14 Aug 23:05	15 Aug 08:00	8.9	-27	0.49	3,200 m	43 m	Yes
11	05 Sep 04:30	05 Sep 08:35	4.1	-25	0.61	NA	30 m	Yes
12	30 Sep 03:30	30 Sep 11:05	7.6	-28	0.46	NA	NA	Yes

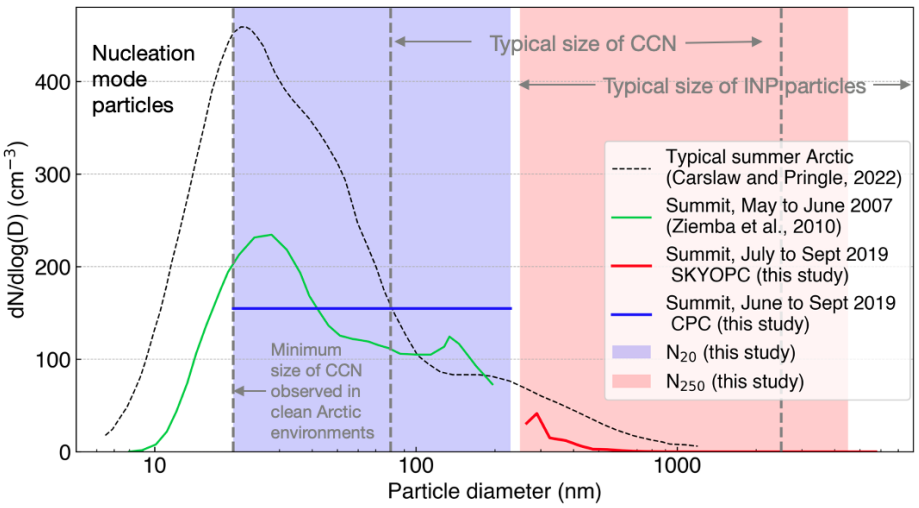

Figure 1. The portion of the aerosol particle size distribution measured in this study, N_{20} shaded in blue and N_{250} in red, overlaid on the typical size distribution of the near-surface Arctic atmosphere in summer (Carslaw, 2022, black dashed line), and the observed size distribution of surface aerosol particles at Summit between May and June 2007 from Ziemba et al. (2010) (green line). The blue and red lines indicate the mean values from the CPC (a single value in the range 20 to 230 nm) and the SKYOPC (size resolved measurements in 20 bins between 250 and 4500 nm) observed between June (or July for the SKYOPC) and September 2019.

3 Retrieval of fog microphysical properties

We use the mixed-phase cloud property retrieval algorithm (MIXCRA, Turner, 2005), which uses optimal estimation to retrieve fog microphysical properties at 5-min intervals from the spectral longwave radiation measured by the AERI (note that we did not apply temporal averaging to the AERI spectra). The longwave radiation is sensitive to changes in cloud/fog phase, particle size, and optical depth when the optical depth is between ∼0.25 and 6, allowing the retrieval of these properties using optimal estimation (Turner, 2005; Cox et al., 2014). As the optical depth approaches the upper end of this range, the longwave spectral signature of the cloud/fog approaches that of a black body and contains little information about microphysical properties. As the optical depth approaches the lower end of this range, the signal to noise ratio of the AERI becomes too low for meaningful retrievals. Figure 2 shows how the mean spectral signature from the AERI during the fog events varied, spanning much of the dynamical range between clear sky conditions and optically thick stratus in the atmospheric window region (where the cloud-free atmosphere is mostly transparent to longwave gaseous absorption ∼800 to 1200 cm^{-1}).

MIXCRA models each fog event as two collocated 'clouds', one consisting of ice crystals and the other of water droplets. Starting from user input a priori values of optical depth (τ) and particle effective radius (R) for each cloud (τ_{liq} and R_{liq} for the liquid cloud and τ_{ice} and R_{ice} for the ice cloud), as well as vertical profiles of atmospheric temperature and water vapor content, the algorithm uses a forward model to calculate the expected spectral signature of the combined cloud and atmosphere, and then iterates using optimal estimation to determine the values [τ_{liq}, R_{liq}, τ_{ice}, R_{ice}] that optimally match the spectral signature observed by the AERI, given the a priori and the measurement uncertainty.

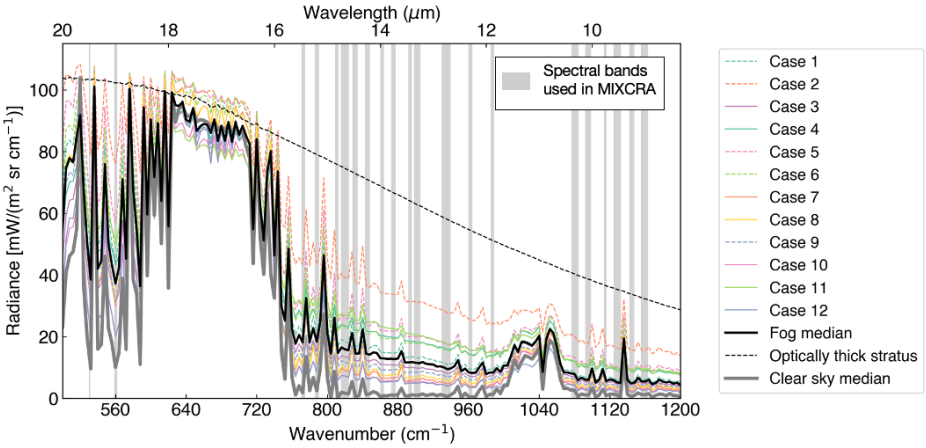

Figure 2. AERI radiance measurements averaged over each fog case (colored lines, see legend inset). The thick black line shows the median for all fog cases, which can be contrasted to the median over all confirmed clear sky hours (thick grey line), and an example of an optically thick stratus cloud (from 01 to 02 UTC on 08 June 2019, dashed black line). Spectral radiance is resampled to 4 cm^{-1} for clarity (native resolution is 0.5 cm^{-1}). Vertical grey lines show the spectral bands used in the MIXCRA retrievals (between major gaseous absorption bands). Note the two spectral bands at wavenumbers below 570 cm^{-1}; these are critical for ascertaining the phase of the fog layers (?, ?; Turner, 2005).

Note that throughout this study τ refers to the visible optical depth (where extinction efficiency is 2), transformed from the optical depth at 11 μm as described in Turner (2005). See Turner (2005) for further information about the implementation of the optimal estimation. After the retrieval of [τ_{liq}, R_{liq}, τ_{ice}, R_{ice}], fog LWP is determined from equation (1), where ρ is the bulk density of water.

$$LWP = \frac{2\rho R_{liq}\tau_{liq}}{3} \tag{1}$$

MIXCRA uses the Line-by-Line Radiative Transfer Model (LBLRTM) version 12.1 (Clough et al., 1992; Clough & Iacono, 1995) as a forward model to calculate the gaseous clear sky optical depth spectra as a function of height, and the DISORT algorithm (Stamnes et al., 1988) to simulate radiance from the ice and liquid cloud (which accounts for both scattering and absorption); the combined LBLRTM and DISORT code is referred to as LBLDIS. The HITRAN 2008 database (Rothman et al., 2009) provides the molecular absorption properties used by the LBLRTM. The single-scattering properties used by DISORT are discussed in section 3.1.1. The radiative transfer calculation also requires information about the thermodynamic structure of the atmosphere and profiles of atmospheric gases. Trace gas concentrations are supplied by the U.S. standard atmosphere (1976), and CO_2 concentrations are scaled to mimic the seasonal and yearly increase in atmospheric CO_2 observed at the Mauna Loa observatory. Uncertainties related to the distribution and concentration of these gases are mitigated in MIXCRA by only including narrow spectral bands (micro-windows) from the AERI in the optimal estimation process, and hence avoiding major gaseous absorption bands (the micro-windows used in this study are highlighted on fig. 2).

Thermodynamic profiles (temperature and water vapor) used within MIXCRA were retrieved using the TROPoe algorithm, which also uses an optimal estimation approach

based on AERI observations, taking advantage of the fact that the AERI is also highly sensitive to the thermodynamic structure of the atmosphere (Turner & Blumberg, 2019; Turner & Löhnert, 2021). The accuracy of the TROPoe thermodynamic profile retrievals during the 12 fog case studies is ± 1.0°C for temperature and ± 0.39 g kg^{-1} for water vapor in the lowest 1,000 m a.g.l (Guy et al., 2022). We assume that any impact of aerosols on the radiative transfer calculation is negligible, because the absorption and scattering coefficients of aerosol particles in the infrared at Summit are generally small (Schmeisser et al., 2018) and there are no local sources of aerosol particles near Summit after instances of local pollution from the station are excluded.

The a priori value of τ_{liq} used as starting point for the optimal estimation is based on the LWP retrieved by the TROPoe algorithm (Guy et al., 2022) with a standard deviation of 6. Note that TROPoe does not account for scattering processes and assumes only liquid droplets are present; MIXCRA adjusts this first guess value to account for the possible presence of ice particles and accounts for multiple scattering. The a priori value for R_{liq} is set to 11 ± 6 μm, based on in-situ measurements of the size distribution of fog droplets at Summit in 2013 and 2014 (Cox et al., 2019). The a priori ice optical depth is set to 0 with a standard deviation of 6, which gives the algorithm flexibility to retrieve ice properties. The choice to initiate the retrieval with a liquid-only cloud is based on the fact that liquid phase fogs are more commonly detected than ice fogs during the summer at Summit (Cox et al., 2019). The a priori ice particle effective radius is set to 18 ± 15 μm based on the distribution of ice crystal effective radius retrieved from mixed-phase clouds over the Arctic Ocean in 1998 (Turner, 2005).

3.1 Uncertainty quantification and quality control

As an initial quality control, we omit any retrievals where the root mean squared error (RMSE) between the final forward radiance calculation (that is, the calculation of expected radiance using the retrieved cloud properties) and the measured AERI radiance is > 1.2 RU. The goal of this quality control is to omit any retrievals for which the retrieval is unable to bring the calculated radiance into agreement with the measured radiance to within the expected instrument uncertainty level (a threshold of 1.2 RU is selected because in 90% of all retrievals the RMSE corresponding to a 3σ uncertainty in the AERI measurements due to noise and calibration uncertainty falls below this value). For rejected retrievals, we assume that additional unknown sources of error exist (e.g. large errors in temperature), hindering accurate cloud property retrievals. Cox et al. (2019) also used a threshold of 1.2 RU for the retrieval of cloud microphysical properties from AERI measurements in northern Canada.

MIXCRA calculates the uncertainties in [τ_{liq}, R_{liq}, τ_{ice}, R_{ice}] by propagating the calibration uncertainty of the AERI ($< 1\%$ of ambient radiance, described in Knuteson et al., 2004a) and the uncertainty associated with the sensitivity of the forward model (i.e. how much the spectral cloud emissivity changes with small perturbations in [τ_{liq}, R_{liq}, τ_{ice}, R_{ice}]) through the optimal estimation algorithm (Turner, 2005). Figure 3 shows how the 2σ percentage uncertainty (as output by the MIXCRA algorithm) varies as a function of τ_{liq} (for τ_{liq} and R_{liq}) and τ_{ice} (for τ_{ice} and R_{ice}) for all the retrievals during the fog events. For all retrieved properties, the minimum percentage uncertainties occur when the fog optical depth is $\sim$1, consistent with the findings of Turner (2005).

The percentage uncertainties in all properties increase when the fog is mixed phase (i.e. when both τ_{liq} and $\tau_{ice} > 0.02$, light blue and pink colours in fig. 3), which is related to the additional degrees of freedom when retrieving properties for a mixed-phase cloud compared to a single-phase cloud as well as the challenges of separating the two phases cleanly (because the liquid and ice signals are correlated). The higher percentage uncertainties in R_{ice} compared to R_{liq} are related to the fact that the retrieval is more sensitive to small particles, and ice particles are generally larger than liquid droplets.

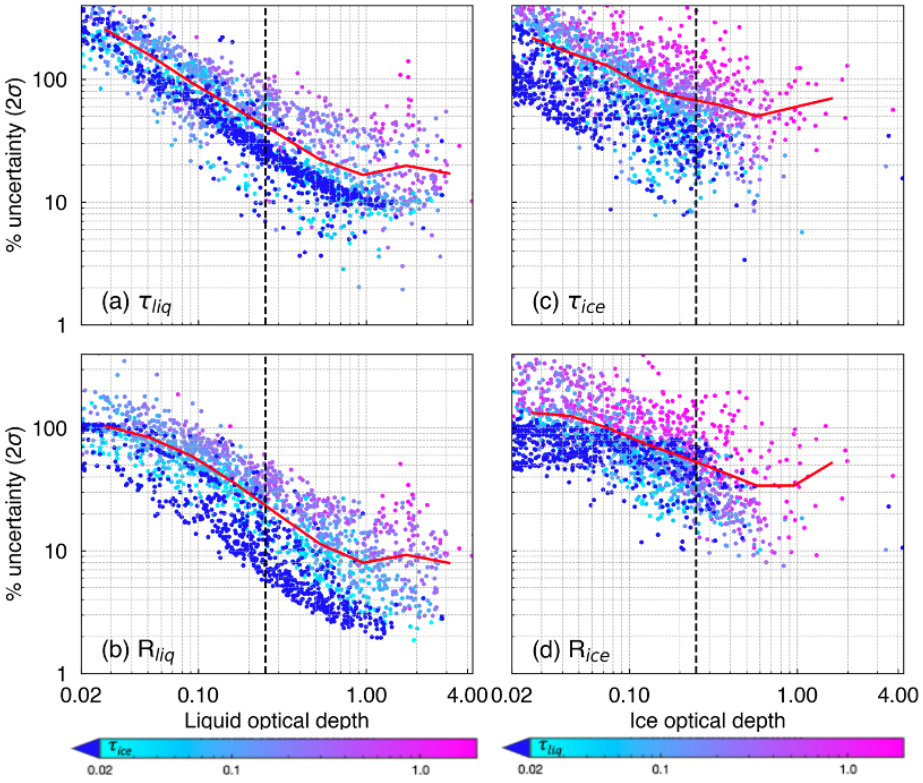

Figure 3. Percentage uncertainty (2σ) in (a) τ_{liq} and (b) R_{liq} as a function of τ_{liq} , and in (c) τ_{ice} and (d) R_{ice} as a function of τ_{ice}, for every retrieval used in this study. The red line is the mean value (in nine logarithmically spaced bins). Points are coloured based on the magnitude of τ_{ice} (a and b) or τ_{liq} (c and d). The black vertical dashed line highlights an optical depth of 0.25 used as a minimum required optical depth for valid retrievals in this study.

As the fog optical depth approaches zero, the percentage uncertainties in all retrieved properties become very large due to the decreasing signal-to-noise ratio, necessitating the selection of a minimum optical depth above which fog microphysical properties can be retrieved with an acceptable level of uncertainty. For this study we choose to use an optical depth threshold of $\tau_{liq} > 0.25$ (for τ_{liq}, R_{liq} and LWP) and $\tau_{ice} > 0.25$ (for τ_{ice}, R_{ice}), consistent with Cox et al. (2014), resulting in a mean 2σ percentage uncertainty of $< 40\%$ for τ_{liq} and $< 20\%$ for R_{liq} (fig. 3). This corresponds to a minimum detectable liquid water path of 2.0-3.0 g m^{-2} (for R_{liq} 12 to 18 μm) with a 2σ uncertainty of 0.9-1.5 g m^{-2}. For ice properties, $\tau_{ice} > 0.25$ corresponds to when the mean percentage uncertainties in τ_{ice} and R_{ice} are below $\sim$60% (fig. 3).

We do not need to be concerned about a loss of sensitivity due to saturation in the infrared, because none of the fog cases have a spectral signature approaching that of a black body (fig. 2). Furthermore, because the maximum precipitable water vapor (PWV) during the 12 fog events is only 0.78 cm (with a mean value of 0.35 cm across all events), the ability of MIXCRA to determine fog phase is not impacted by excessive water vapor ($>$ 1 cm PWV can lead to signal saturation in the 16 to 20 μm region, Turner, 2005; Cox et al., 2014). Figure 4 shows the percentage of retrievals during each case study that meet the quality control criteria of RMSE < 1.2 RU and $\tau_{liq} > 0.25$ (for liquid phase retrievals) or $\tau_{ice} > 0.25$ (for ice phase retrievals). Less than 8% of all retrievals are discarded due to poor RMSE, but the optical depth threshold severely limits the percentage of valid retrievals in each fog case, and in case 7, the optical depth is too low for any valid retrievals.

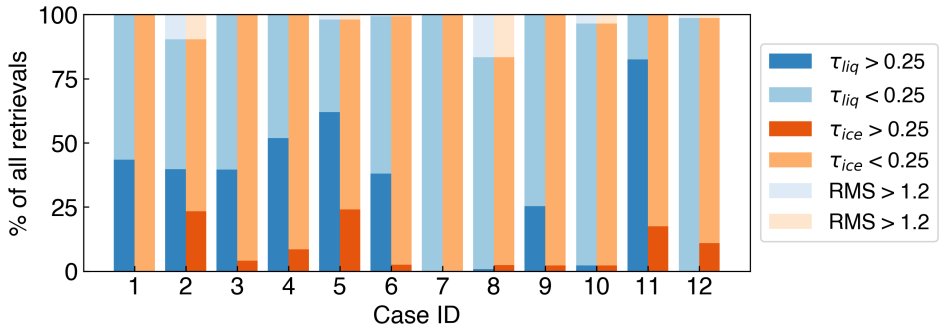

Figure 4. The percentage of all retrievals from each case study that meet the quality control criteria of RMSE < 1.2 and optical depth > 0.25 for liquid properties (blue) and ice properties (orange). The percentage of good retrievals used in the remainder of this study are shown by the dark blue and orange colours.

The MIXCRA algorithm does not account for uncertainties in the atmospheric state (gas and temperature profiles) or for uncertainties related to the choice of single-scattering properties (SSPs) for liquid droplets and ice crystals. As mentioned above, uncertainties related to the concentrations of atmospheric gases are minimised through the selection of micro-windows used by MIXCRA. The atmospheric temperature profile has a mean RMSE (compared to radiosonde profiles) of ± 1°C in the lowest 1,000 m a.g.l during these case studies (Guy et al., 2022), and the difference in the retrieved values of [τ_{liq}, R_{liq}, τ_{ice}, R_{ice}] if the temperature profile is uniformly increased or decreased by 1°C are small, resulting in a mean difference in τ_{liq} of 0.2 and R_{liq} of 0.8 μm based on sensitivity tests with 38 retrievals.

3.1.1 Uncertainties related to the choice of SSPs

The choice of single-scattering properties (SSPs) to use in the retrievals is non-trivial. There is emerging evidence that the SSPs of supercooled water droplets are temperature dependent, and that the use of SSPs that assume a warmer temperature than reality can result in overestimations of ice fraction and underestimations of liquid droplet effective radius (Rowe et al., 2013, 2022). Although the temperature profile during the fog events is well characterised, the temperature during a single event can vary by up to 13°C both temporally and vertically within the lowest 15 m a.g.l due to radiative cooling and changes in boundary layer mixing (fig. S1, supporting information). Furthermore, the SSPs of ice crystals depend on the ice crystal habit (e.g. Yang et al., 2005), but there is very little information about ice crystal habit at Summit during fog events. Isolated plates and bullets are often reported by observers, but whether any of these crystals are associated with fog events (as opposed to snow, blowing snow, or diamond dust) is unclear. A multi-angled snowflake camera operational at Summit in 2019, which photographed particles with a maximum dimension > 30 μm (Garrett et al., 2012), did not detect any identifiable ice crystals during the fog events. This suggests that any ice particles that were present during the fog were unlikely to be bullets or columns, which are typically > 30 μm along their major axis (Walden et al., 2003). Schmitt et al. (2013) found that ice fog particles in the interior of Alaska are generally droxtals or plates, although these fogs are not necessarily comparable to Summit because they were heavily polluted.

To account for the additional uncertainty related to the choice of SSPs, we ran MIXCRA in three configurations (P_w, P_c, and D_w; Table 2). We choose from four databases of liquid droplet SSPs corresponding to temperatures of 240, 253, 263, and 273 K (Rowe et al., 2013, 2020). For P_w and D_w, we use the liquid SSPs that correspond to the warmest temperature measured in the lowest 15 m a.g.l during each fog event, and for P_c we use the liquid SSPs that correspond to the coldest temperature measured during the fog (fig. S1). For the ice habit, we use SSPs associated with hexagonal plates (for P_w and P_c) and droxtals (for D_w) (Yang et al., 2005). We choose these three configurations as a compromise between reducing the computational time of running multiple configurations and representing the uncertainty associated with the SSPs well. Results from individual test cases indicated that changing the liquid SSPs between the warmest and coolest temperatures had a larger impact on the results than changing the ice SSPs.

Table 2. The three configurations of single-scattering properties (SSPs) for ice and liquid particles used in the MIXCRA retrievals. Liquid SSPs at temperatures of either 240, 253, 263, or 273 K were used, corresponding to the warmest (or coldest, per table) measured temperature in the lowest 15 m a.g.l. during each fog event.

	Ice habit	Liquid SSP temperature
P_w	Plates	warmest
P_c	Plates	coldest
D_w	Droxtals	warmest

For the rest of this study, the microphysical retrievals shown are the mean values of the three configurations in Table 2, and we account for the additional uncertainty introduced by the SSPs assumption using equation (2), where 2σ is the combined uncertainty of each retrieved parameter (i.e. τ_{liq}, R_{liq}, τ_{ice}, and R_{ice}), $2\sigma_a$ is the 2σ uncertainty output by the MIXCRA algorithm, ΔS_i is the maximum difference in the retrieved parameter resulting from varying the ice crystal SSPs, and ΔS_L is the maximum difference in the retrieved parameter resulting from varying the liquid SSPs.

$$2\sigma = \sqrt{2\sigma_a^2 + \Delta S_i^2 + \Delta S_L^2} \tag{2}$$

3.2 Validation against in-situ measurements

The ability of the MIXCRA algorithm to accurately determine simultaneous ice and liquid optical depths of single-layer mixed-phase Arctic clouds is well established through comparisons with depolarisation lidars (Turner et al., 2003; Turner & Eloranta, 2008), but assessments of the accuracy of MIXCRA retrievals of cloud droplet effective radius are limited to two comparisons with in-situ aircraft measurements of liquid-phase stratus clouds over the south-central US (Vogelmann et al., 2012) and off the west coast of California (Turner, 2007). Vogelmann et al. (2012) found that MIXCRA captured the primary mode of the cloud droplet distribution well; the mean and standard deviation of the MIXCRA size distribution was 5.3 ± 1.6 μm compared to 4.9 ± 0.7 μm for the aircraft probe. Turner (2007) found a mean bias of 0.1 μm between the aircraft measurements and MIXCRA, with an interquartile spread of 1.9 μm. In both cases, the aircraft measurements represent just one level in the cloud whereas the MIXCRA retrievals are representative of a column value (weighted by optical depth). To date, there have been no assessments of the accuracy of MIXCRA in determining the microphysical properties of fog.

Here, we assess the ability of MIXCRA to retrieve R_{liq} during fog at Summit by comparing MIXCRA R_{liq} retrievals with droplet effective radius determined from FM100 single-particle light scattering spectrometers installed at 2 m and 10 m a.g.l during a supercooled liquid fog event at Summit on 16 June 2013 (fig. 5). Note that the FM100 instruments were installed on a tower approximately 480 m from the AERI instrument. This case is described further in Cox et al. (2019) and is a near-idealised example of radiation fog formation at Summit, the development of which is particularly similar to case 4 in 2019.

The FM100 probes made size-resolved measurements of particles with radii (r) of 1-25 μm based on individual particle scattering characteristics, under the assumption that the particles are liquid spheres. The effective radius (R) was calculated from the FM100 particle size distribution [n(r)] using equation (3).

$$R = \frac{\int_0^\infty \pi r^3 n(r) dr}{\int_0^\infty \pi r^2 n(r) dr} \tag{3}$$

To estimate the uncertainty in R determined from the FM100 measurements, we recalculated the FM100 particle size distribution 100 times, each time randomly selecting errors from uniform distributions of five possible sources of uncertainty: (1) probe air speed (±5%), (2) wind speed (±0.5 m s^{-1}), (3) wind direction (±5°), (4) whether or not overlapping bins were combined (as described in Cox et al., 2019) (binary), and (5) the uncertainty in bin sizing (randomised shifts to neighbouring bins). For more details on the uncertainties associated with the FM100 probe, see Cox et al. (2019) and supplement. Bin sizing ambiguities were dominant over sampling errors for this case because the latter were small due to the ambient wind direction and speed being optimally aligned with the probe inlet geometry and the speed of the pumped air through the probe (see also Spiegel et al., 2012). The 2σ uncertainty in R is then determined from the standard deviation of R across all the perturbed calculations.

MIXCRA R_{liq} is not directly comparable to R determined from the FM100 probes, because the downwelling radiance measured by the AERI is sensitive to the bulk infrared signal from the entire population of particles in the scene view of the AERI instrument (the height of which varies with accumulation but is typically around 3 m a.g.l), whereas R determined from the FM100 is based on the forward scattering of light in the visible

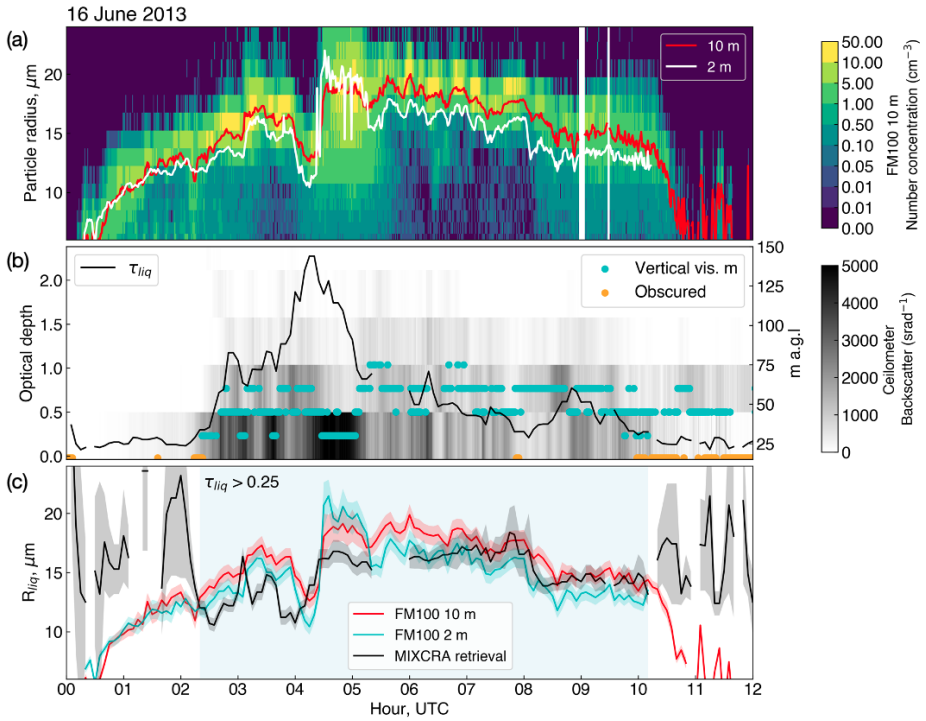

Figure 5. Fog event on 16 June 2013. (a) Calculated effective radius (R) from FM100 measurements at 10 m a.g.l (red line) and 2 m a.g.l (white line) overlaid on the FM100 particle size distribution at 10 m a.g.l. (coloured shading). (b) Retrieved liquid optical depth (black line), raw ceilometer backscatter (grey shading), and ceilometer vertical visibility values (blue markers, and orange for 'obscured'). (c) Cross validation of fog droplet R_{liq} retrieved from the MIXCRA algorithm (black) and determined from in-situ measurements (FM100 probes at 2 m, cyan, and 10 m, red). Shading represents 2 σ uncertainties, and the light blue region shows where the retrieved optical depth was greater than 0.25.

range from individual particles passed across the detector at a set height above the surface (2 m or 10 m). Therefore, we would only expect these values to compare well if the size distribution of the particle population at the height of the FM100 instrument was representative of the vertical distribution of the particle population. Cox et al. (2019) show that the fog droplet size distribution varies with height, with the 2 m probe generally measuring larger particles than the 10 m probe, consistent with particles preferentially forming higher up before settling out. However, on 16 June 2013, after the initial fog formation, the R at 2 m was consistently smaller than at 10 m (fig. 5), the particle number concentration at 2 m was also consistently higher than at 10 m (Cox et al., 2019), possibly indicating partial evaporation of droplets and a reduction in settling velocity at 2 m.

Despite this caveat, the MIXCRA R_{liq} compares very well to the R calculated from both FM100 probes when $\tau_{liq} > 0.25$ (fig. 5c) over a range of R from 12.5 to 20 μm. The RMSE between the MIXCRA R_{liq} and FM100 R is 2.0 μm at both 2 m and 10 m, with a Pearson's correlation coefficient of 0.57 and 0.69 respectively. However, the strength of this correlation is not consistent over the fog lifetime. During the initial stage of the fog (02:20 to 04:00) the MIXCRA R_{liq} was consistently smaller than R from both FM100 instruments (by an average of 1.5 μm at 2 m and 2.7 μm at 10m). Between 04:00 and 05:00 there was an initial reduction in R in the FM100 measurements (and a reduction in particle number concentration, Cox et al., 2019) followed by a sharp increase in R at 04:15. This coincided with a sharp increase in optical depth (fig. 5b), erosion of the surface temperature inversion, and evidence of wind-shear driven mixing in sodar observations (Cox et al., 2019). The increase in R was also apparent in the MIXCRA R_{liq}, but started earlier (at 04:00), and the maximum R_{liq} between 04:30 and 05:00 (17 μm) was lower than the maximum R measured by the FM100 probes during this interval (21 μm at 2 m and 19 μm at 10 m). This could be explained by an increase in altitude of the main layer of droplet formation; when the optical depth increases and the surface-based temperature inversion is eroded, new droplet formation would be initiated by radiative cooling at the fog top (Haeffelin et al., 2013). If the droplet formation layer height increased to greater than 10 m a.g.l, these droplets would have then grown and settled, resulting in larger particles at 10 m and even larger particles at 2 m (as observed between 04:30 and 05:15). After 05:15, the fog LWP decreased (Cox et al., 2019) suggesting no further droplet growth, and the optical depth gradually decreased. Between 06:00 and 10:00, the boundary layer was well-mixed (Cox et al., 2019), R varied consistently at 2 m and 10 m, and the MIXCRA R_{liq} captured these variations well. Overall, the MIXCRA R_{liq} is slightly better correlated with the measurements at 10 m, although this is largely due to detection of large (> 20 μm) particles detected at 2 m that are not reflected in the MIXCRA retrieval.

In summary, this cross-validation demonstrates that the MIXCRA algorithm can accurately retrieve R_{liq} during fog events at Summit with the following caveats:

1. Due to the threshold optical depth of 0.25, below which signal to noise ratio in the AERI measurements is insufficient to accurately retrieve fog microphysical properties, MIXCRA is not able to capture the initial growth period of the fog droplets (between 00:10 and 02:20 in fig. 5).
2. These results are based off a single case study and cover an effective radius range of 12.5 to 20 μm. More observations of R at a variety of heights and over a larger range of fog conditions are necessary to fully characterise the ability of MIXCRA to accurately retrieve fog droplet effective radius.

4 Results

4.1 Summary of microphysical retrievals during the 2019 fog cases

Figure 6 summarises the retrieved fog microphysical properties from the twelve case studies, and figures S2 and S3 in the supporting information show the temporal evolution of the microphysical properties during each case. Retrievals were calculated every five minutes during each fog event, so the number of valid retrievals indicated on fig. 6a is the number of five-minute intervals during which there was sufficient optical depth for the retrieval ($\tau_{liq} > 0.25$ for liquid, or $\tau_{ice} > 0.25$ for ice properties).

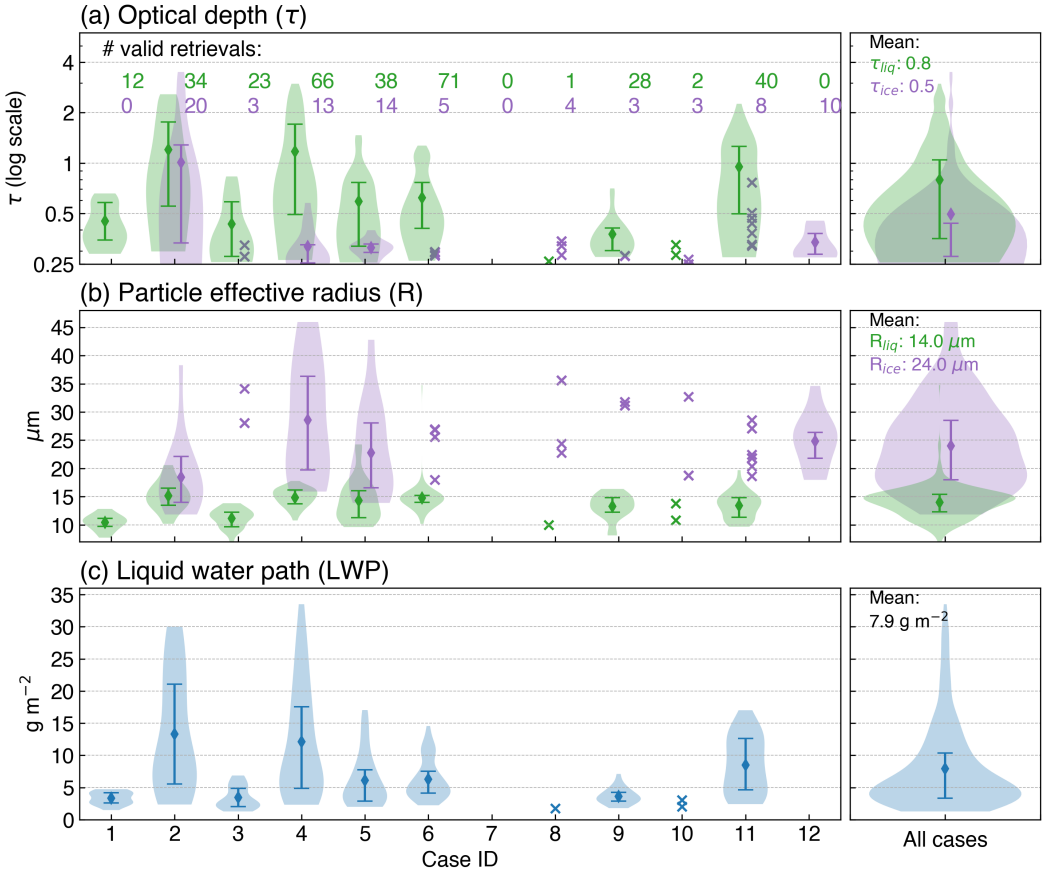

Figure 6. Relative probability distribution of fog microphysical properties retrieved during each individual case study listed in table 1 and for all cases (right hand side). The mean and interquartile range of each distribution is shown by the diamond shaped point and associated error bars when the number of valid retrievals is > 10, otherwise crosses show values from individual retrievals. (a) Liquid (τ_{liq}, green) and ice (τ_{ice}, purple) optical depth, (b) liquid (R_{liq}, green) and ice (R_{ice}, purple) particle effective radius, and (c) liquid water path (LWP). Only retrievals where the optical depth is sufficient are shown ($\tau_{ice} > 0.25$ for ice properties, or $\tau_{liq} > 0.25$ for liquid properties).

For the cases where there was sufficient ice optical depth for a retrieval, the mean R_{ice} was 24.0 μm (fig. 6b) and the range was 18.5 to 31.4 μm. This is in broad agreement with the mean effective radii of ice crystals measured in low-level Arctic clouds (~21-25 μm, Lawson, Baker, Schmitt, & Jensen, 2001; Turner et al., 2003; McFarquhar et al.,

2007). The mean R_{liq} was 14.0 μm and the mean during individual events varied from 10.0 to 15.1 μm (fig. 6b). The overall mean R_{liq} is slightly larger than the mean R determined from the summertime FM100 measurements at 10 m in 2013/14 from Cox et al. (2019), which was 11.4 $\pm$ 3 μm. However, it is important to note that the MIXCRA retrievals are only valid when $\tau_{liq} > 0.25$, and hence they do not include the initial phase of fog formation where there are a lot of very small droplets that can be detected by the FM100 (for example, see fig. 5). The range in R_{liq} across all retrievals was 6.6 μm (at the beginning of case 3) to 34.8 μm (just prior to fog dispersal in case 6).

Most of the fog cases have a mean LWP < 10 g m^{-2} (fig. 6c), but for cases 2 and 4 the maximum LWP exceeds 30 g m^{-2}, which can result in an increase in downwelling longwave radiation of > 50 W m^{-2} relative to clear sky conditions (Miller et al., 2015; Cox et al., 2019). The minimum LWP retrieved by MIXCRA was 1.3 g m^{-2} at the beginning of event 3, associated with the smallest retrieved droplet size (R_{liq} 6.6 μm). In cases 7, 8, and 10, the fog is so optically thin that the LWP is below the limit of detection for most of the event despite a reduction in horizontal visibility at the surface (to just 400 m in case 8) and observations of fog bows confirming the presence of liquid water on all three occasions. No optics were reported by onsite observers during the ice-phase fog (case 12), although the sun was below the horizon most of the time.

4.2 Aerosol particle measurements during fog events

The mean N_{250} across all fog events was 1.7 cm^{-3} (with the mean during individual events ranging from 0.4 to 2.2 cm^{-3}, fig. 7a), and the mean N_{20} across all fog events was 187 cm^{-3} (ranging from 41.9 to 448 cm^{-3}, fig. 7b), these values represent the interstitial aerosol particle number concentration during fog. The temporal evolution of N_{20} and N_{250} during each event is shown in fig. S4 in the supporting information. The mean N_{250} during fog events is slightly lower than the overall mean value (including clear and foggy periods) from June to September 2019 (2.4 cm^{-3}), whereas the mean value of N_{20} during fog is slightly higher than the seasonal mean (170 cm^{-3}). However, the mean N_{250} and N_{20} over the 2 hours prior to fog onset are 8.2 and 191 cm^{-3} respectively, both of which are higher than the mean values over the entire period. In all but case 7, N_{250} drops below 0.5 cm^{-3} during the fog event, suggesting that almost all particles in the N_{250} size range are activated into (or scavenged by) fog particles. This is not the case for N_{20}; an order of magnitude decrease in N_{20} during fog is only apparent in case 10, where N_{20} falls below 10 cm^{-3}.

Figure 8 illustrates the temporal evolution of N_{250} and N_{20} during each fog event, where fog onset is defined as when the downwelling radiance measured by the AERI increases above the clear sky threshold (see section 2.2), and the percentage change in N is relative to the mean value during the two hours prior to fog onset. On average, both N_{250} and N_{20} decrease during the first 300 minutes after fog onset, consistent with the growth and activation of aerosol particles into fog particles that are too large for either instrument to detect (> 6 μm). Note that this does not necessarily mean that these particles are removed from the atmosphere; they may sediment out or they may be released back into the atmosphere after the fog evaporates, either in the same form or after processing within the fog particle.

For N_{250} there is a reduction in number concentration after fog onset in all events (of 72 $\pm$ 26% after 300 minutes). For case 12, the magnitude of the percentage decrease is small compared to the other events, which is related to the fact that the absolute values of N_{250} during case 12 are exceptionally low, with an initial mean N_{250} in the two hours prior to fog onset of only 0.2 cm^{-3}. The initial N_{250} in the 2 hours prior to fog onset is consistent in time for all cases apart from case 11, where it varies between 1.2 and 6.8 cm^{-3}. In cases 8 and 10, a sharp reduction in N_{250} of 80% begins 30 minutes prior to the radiative detection of fog onset, whereas in cases 3 and 7, there is a slight

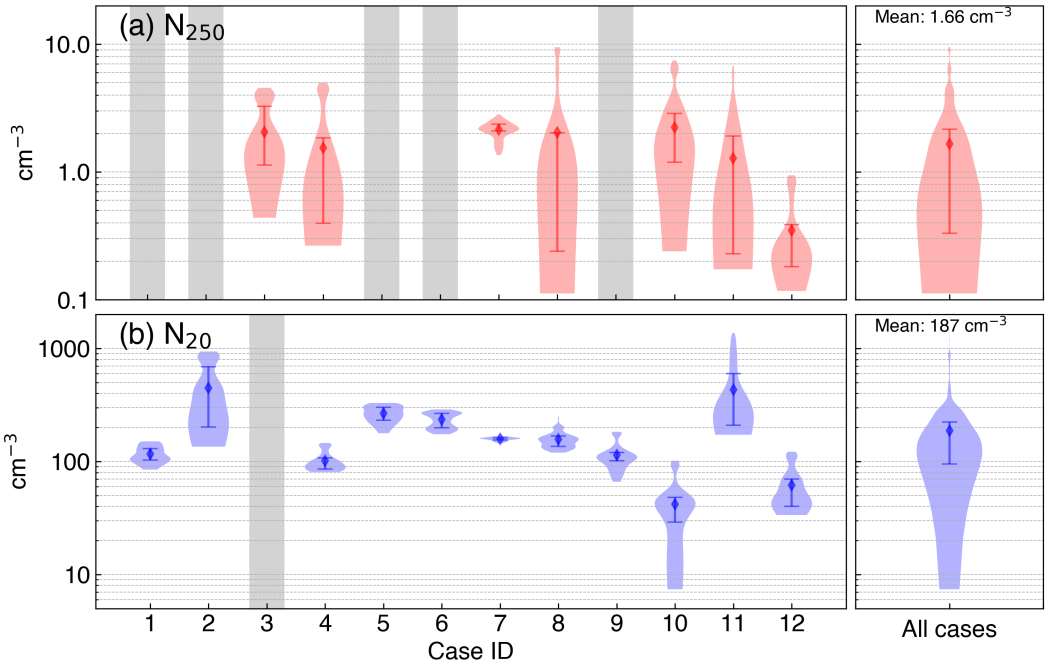

Figure 7. Relative probability distribution of aerosol particle number concentrations [(a) N_{250} and (b) N_{20}] measured during each individual case study listed in table 1 (left) and for all cases (right). The mean and interquartile range of each distribution is shown by the diamond shaped point and associated error bars. Grey bars indicate missing data (< 80% complete during fog event).

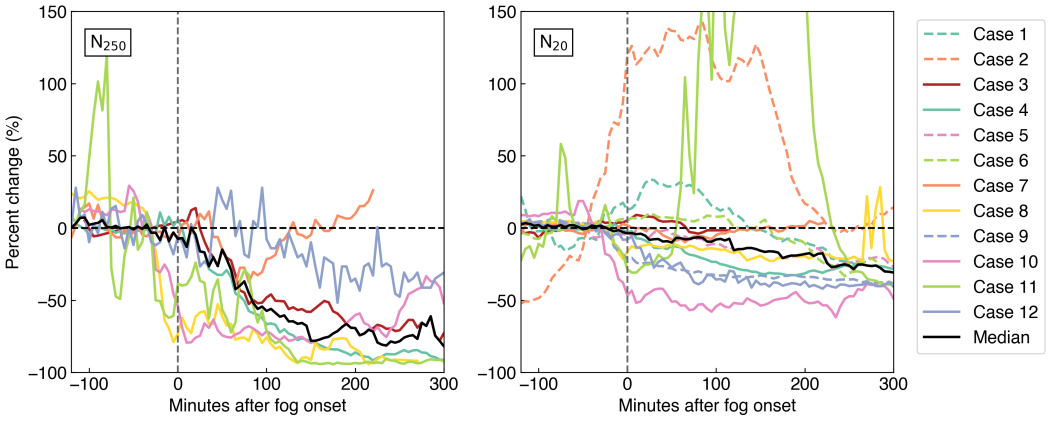

Figure 8. Percent change in N_{250} (left) and N_{20} (right) during the first 300 minutes of each fog event (coloured lines, see legend inset), compared to the average value in the two hours prior to fog onset. Thick black line is the median across all events.

increase in N_{250} at fog onset followed by a reduction in N_{250} that starts 20-30 minutes later. The duration of case 7 is only 102 minutes in total, and 80 minutes into the event N_{250} begins to increase, returning to the concentration prior to fog formation 10 minutes after the fog is no longer detected, suggesting that on this occasion, 100% of the particles that were incorporated into the fog were re-released after the fog dissipated.

In contrast to N_{250}, the change in N_{20} is highly variable between different fog events (fig. 8). In cases 2 and 11, there was more than a 100% increase in N_{20} during the event. For case 2, this increase started two hours before the fog was detected, meaning that the 'initial' N_{20} concentration is not a good representation over average conditions prior to the fog. In case 11 there was an initial decrease in N_{20} followed by a sharp increase 60 minutes into the fog event, during which N_{20} reached 1370 cm^{-3} (> 99th percentile of N_{20} measured between June and September 2019), but 240 minutes later, after the fog was no longer detected, N_{20} returned to values close to those prior to fog onset. This anomalous case is discussed further in section 5. In cases 8, 9, and 10, there was a reduction in N_{20} that started 30-40 minutes prior to fog onset (of 20%, 30%, and 50% respectively).

Note that some of the variability in evolution of N_{20} during fog events could be related to the size distribution of N_{20} particles; for example, if most of the N_{20} particles are closer to 30 nm diameter (i.e. the first mode in the Ziemba et al., 2010 measurements, fig. 1) these particles might be subject to different processes during a fog event than to N_{20} particles closer to 150 nm (the second mode in the Ziemba et al., 2010 measurements, fig. 1). Particles closer to 150 nm in size more readily act as CCN, whereas smaller particles would require larger supersaturations before activation. Size resolved measurements of particles < 250 nm diameter would be required to investigate these details further.

For five of the six cases where both N_{250} and N_{20} are available, the two measurements are positively correlated (fig. 9). The exception is case 11, during which N_{250} decreases to < 0.2 cm^{-3}, but there was an anomalous spike in N_{20} in the middle of the fog event (discussed further in section 5). In cases 4 and 8, N_{250} was almost completely depleted, but there is only a small reduction (< 35%) in N_{20}. This suggests that during these two cases, the supersaturations were not high enough to activate many particles with diameters < 250 nm. In cases 10 and 12, N_{250} was almost completely depleted, and N_{20} was also depleted by 73 and 41% respectively. During case 10, the reduction in N_{20} occurred simultaneously with the reduction in N_{250} (fig. 9) even though the initial N_{250} concentration was above average. The reduction in N_{20} and N_{250} started 30 minutes prior to fog detection, and then both concentrations remained steady after fog onset, suggesting that supersaturations during this event were high enough to activate smaller particles (or that the N_{20} concentration in this case was dominated by larger particles). In case 12 the initial concentration of N_{250} was only 0.24 cm^{-3}, and there was a gradual decrease in N_{20} after fog onset.

5 Discussion: Observational evidence of fog-aerosol interactions

The results described in section 4 hint that there are a variety of different ways in which fog interacts with the surface aerosol particle population across the twelve case studies. Of the seven cases for which N_{250} measurements are available, only cases 4 and 11 develop a LWP > 10 g m^{-2}. The longwave radiative forcing for a LWP of 5 to 30 g m^{-2} compared to that of an equivalent clear sky day is very sensitive to small changes in LWP, and the difference between a LWP of 5 g m^{-2} and a LWP of 10 g m^{-2} can equate to > 20 W m^{-2} difference in longwave radiation at the surface (Miller et al., 2015). For this reason, understanding why some fogs develop a LWP > 10 g m^{-2} while others do not is important for understanding the radiative impact of fog over the GrIS. One of the factors that can influence LWP in liquid and mixed-phase fogs is the properties of the aerosol population. In this section, we use the observations presented in section 4 to discuss the role of fog-aerosol interactions over central Greenland. Throughout this discus-

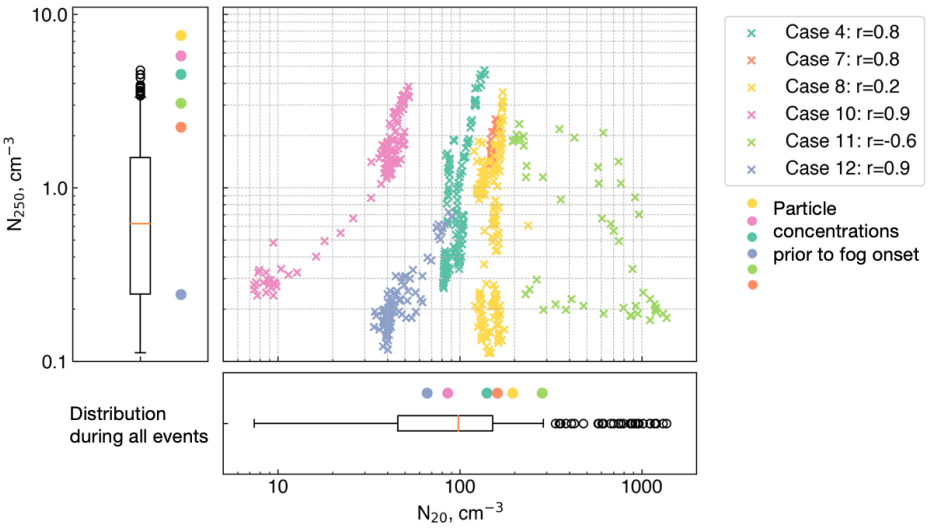

Figure 9. The relationship between N_{20} and N_{250} during the fog events for which both measurements are available. Boxplots show the aggregated distribution of N_{250} and N_{20} during all events. Coloured circles on the boxplots indicate the initial N_{20} and N_{250} concentration averaged over the 2 hours prior to each event. Pearson's-r correlation coefficients (r) in the legend inset are for the correlation between $\log(N_{20})$ and $\log(N_{250})$, all r values are significant at the 99% confidence level.

sion we make the assumption that changes in the fog and aerosol population were occurring in-situ (i.e. not related to advective processes). We justify this assumption based on the fact that (a) most of the fog events are likely to be radiation fogs due to the fact that they form in the evening on days with clear skies, and (b) that the wind speeds (2 to 14 m a.g.l) during all events are relatively low (3.5 ± 0.3 m s^{-1}). Despite the low wind speeds, for some of the longer events ($>$ 8 hours) the horizontal length scale can be $\sim$100 km, and we acknowledge that advective process may have played a role in some of the observed changes in fog and aerosol properties.

5.1 Aerosol particle controls on fog microphysics

The goal of this section is to identify whether there is observational evidence that low aerosol particle number concentrations is a critical control on fog liquid water path and lifetime. To do this, we focus on the cases of liquid and mixed-phase fog where N_{250} measurements are available (cases 3, 4, 7, 8, 10, and 11).

In radiation fog, liquid droplets form when the surface cools radiatively until the air becomes saturated with respect to water, after which water condenses on CCN particles, growing them into fog droplets (e.g. Gultepe et al., 2007). Whether or not ice is present, liquid droplets will continue to grow as long as supersaturation with respect to water is maintained (either by continued radiative cooling or moisture influx) until they are large enough to settle out, and new droplet formation will continue as long as there are CCN particles present that may be activated for the given degree of supersaturation. In the initial stages of radiation fog development, when the atmosphere is stable and close to saturation, the degree of supersaturation is determined by the cooling rate, and by the properties of the aerosol particle population, which determine the number concentration of CCN for a given supersaturation. The air mass specific humidity also plays a role in determining the amount of cooling required to reach a given supersaturation,

but this effect is small because the saturation mixing ratio does not change much at cold temperatures (< 0.1 g kg^{-1} °C^{-1} for temperatures <-8 °C). Based on this, and assuming an absence of advective processes and limited turbulent mixing, the initial formation of liquid droplets in a supercooled radiation fog development might either be 'aerosol-limited' or 'cooling-rate limited' (similar to how a convective cloud might be 'aerosol-limited' or 'updraft limited', i.e. Reutter et al., 2009).

In a 'cooling-rate limited' scenario, the initial supersaturation would increase slowly. Using the observations available in this study, this situation would be characterised by relatively low activated fractions of N_{250} at fog onset, because particles that can act as CCN at low supersaturations will be a subsample of N_{250} (McFiggans et al., 2006), followed by a gradual droplet growth and continual activation while cooling continues, and higher supersaturations allow the activation of further particles. In contrast, an 'aerosol-limited' fog would be characterised by high initial activation ratios of N_{250} and N_{20} at fog onset, as all particles that can act as CCN are activated. With continued cooling, and in the absence of new droplet formation due to a lack of CCN, the existing fog droplets would grow to relatively large sizes, ultimately settling out and preventing an increase in fog LWP despite continued cooling (as described by Mauritsen et al., 2011). The presence of 'aerosol-limited' fogs would support the hypothesis that the low aerosol particle number concentrations can be a critical control on fog liquid water path and lifetime.

To identify whether there are any cases of 'aerosol-limited' fogs, we calculate cooling rates during each fog event from temperature measurements at 2 m, 4 m, 9 m and 14 m a.g.l. The development of the near surface temperature profile during each fog event is shown in the supporting information (fig. S1). The cooling rate is calculated from the 60-minute rolling mean of the mean temperature across these four heights. Of the six cases for which N_{250} measurements are available and liquid water is detected, case 7 has an extremely low cooling rate (< 0.5 K h^{-1}, fig. 10a) and a low activated fraction of N_{250} at fog onset (fig. 8), suggesting that this event is more likely to be limited by the low cooling rate than by the aerosol population.

For the remaining five cases, the maximum cooling rate ranges from 2.4 K h^{-1} (case 11) to 4.0 K h^{-1} (case 10) and occurs 30 to 50 minutes after fog onset, except in case 3, where the maximum cooling rate occurs 140 minutes after fog onset (fig. 10a). These cooling rates are within the range of those observed in mid-latitude radiation fogs ($\sim$1 to 4 K h^{-1}, e.g. Price, 2011; Haeffelin et al., 2013). In cases 3 and 4, N_{250} decreases gradually as the surface layer continues to cool, which suggests that neither of these two cases were in the 'aerosol-limited' regime, and that aerosol number concentrations were not the main reason why case 4 developed into an optically thick fog with LWP > 10 g m^{-2} but case 3 did not. The near-surface specific humidity and temperature profiles in both cases were similar (see table 1), and so the difference in fog development was likely due to differences in dynamics: In case 3, 110 minutes into the event, a burst of turbulent kinetic energy (0.3 m^2 s^{-2}, not shown) at 14 m is followed by warmer temperatures propagating downwards towards the surface (fig. S1), this mixing of warm air downwards could have limited the fog development.

In cases 8 and 10, there is a high activated fraction of N_{250} at fog onset (68 and 62% respectively) as well as a relatively high activated fraction of N_{20} (15 and 45% respectively). Case 10 had the highest activated fraction of N_{20} out of all fog cases. In both cases, there is little further change in N_{250} or N_{20} after fog onset despite continued cooling (figs. 8 and 10). This suggests that the aerosol particle number concentration could have limited fog development (lifetime and LWP) in these cases. Unfortunately, the low fog optical depths limit the ability of the MIXCRA retrieval algorithm to provide information about fog phase and particle sizes for both cases. Finally, in case 11, there is greater variability in N_{250} both prior to and after fog onset compared to the other cases, and in this case the fog develops much more rapidly than in case 4, with LWP increasing to > 10 g m^{-2} 80 minutes after fog onset (as opposed to 180 minutes in case 4). The warm-

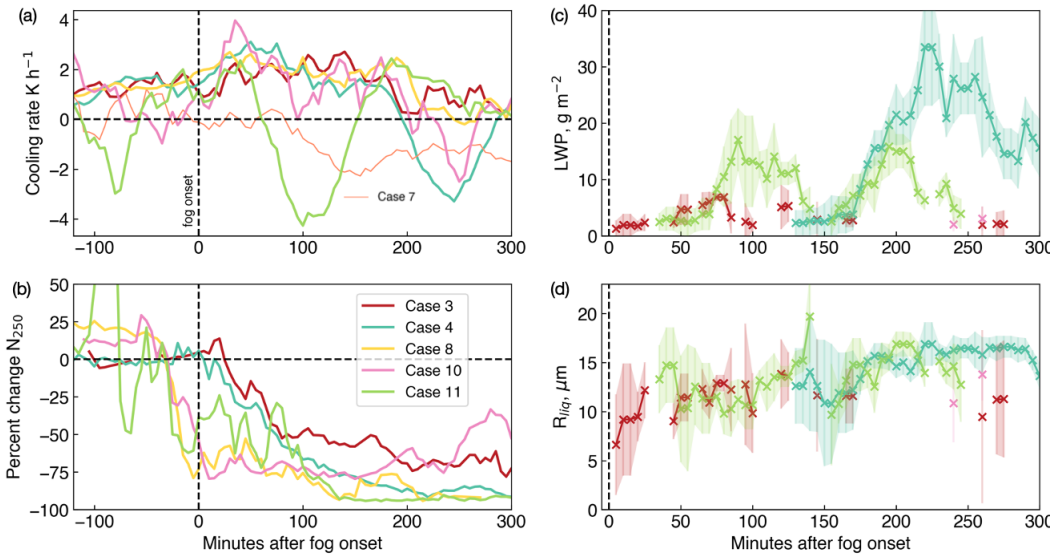

Figure 10. Time series of (a) cooling rate (2 to 14 m a.g.l), (b) percentage change in N_{250}, (c) liquid water path (LWP), and (d) Liquid droplet effective radius (R_{liq}) during the case studies for which N_{250} measurements are available. Note that cases 7 and 12, identified as 'cooling-rate limited' fogs are only included on panel (a). The error bars on panels (c) and (d) show the 2σ uncertainties in the MIXCRA retrievals.

ing of the surface layer that coincides with the sharp increase in LWP is indicative of a transition from near-surface radiative cooling to radiative cooling at fog top maintaining the fog. This case is discussed further in section 5.2.

5.2 Increase in N_{20} associated with fog

We focus on case 11 to look for evidence to support the hypothesis that fog can act to increase surface aerosol particle number concentrations by enhancing mixing of air from above into the near-surface stable layer. Case 11 was anomalous out of the 12 cases because of the exceptionally high N_{20} that occurred during the fog event (1370 cm^{-3}, $>$ 99th percentile of all N_{20} measurements made between June and September 2019), and because it consisted of two distinct phases; the LWP increased from 2.4 g m^{-2} to 17.0 g m^{-2} between 05:05 and 06:00, then decreased to 2.6 g m^{-2} at 07:05 before increasing again to 15.9 g m^{-2} at a 07:45.

The fog formed initially as the near surface temperature cooled after the dissipation of a mixed-phase cloud (with a base height of approximately 1.3 km) at 04:30. But only 80 minutes after fog onset, near surface air temperatures started to increase, and the fog optical depth and LWP started to increase rapidly (fig. 11). Because the surface temperature was no longer decreasing, the increase in fog optical depth and LWP after 05:15 must have been due to a transition from surface radiative cooling to cooling higher in the atmosphere (i.e., radiative cooling at fog top).

If the increase in near-surface air temperature was radiatively driven, we would expect the temperature increase to start closest to the surface first (for example, as in case 2 and 4, fig. S1). The fact that the near-surface air temperature increased simultaneously at each of the four heights (fig. 11d) suggests that another mechanism was responsible. This could have been the advection of a warmer air mass, but the consistent wind direction (90% of all winds measured at 2, 4, 9, and 14 m come from 156° to 222°) and

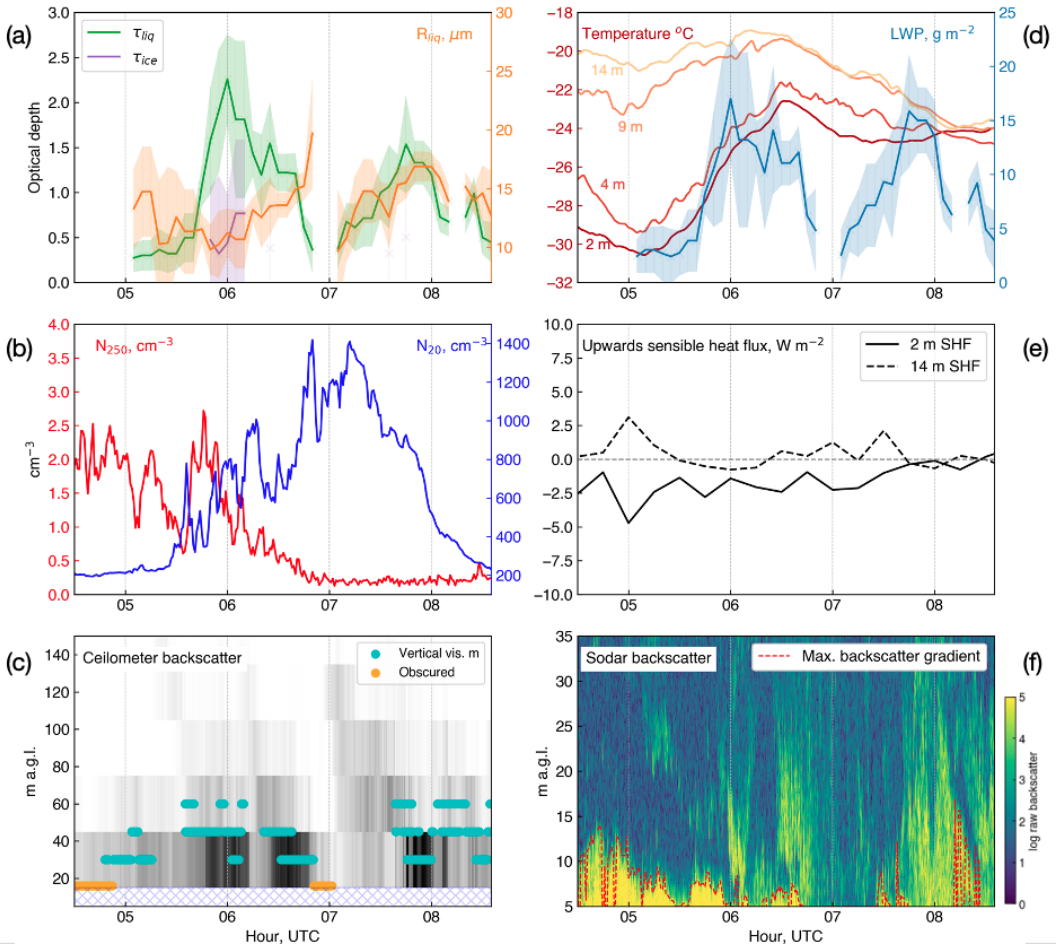

Figure 11. Atmospheric conditions during Case 11 (05 September 2019). (a) Fog optical depth (τ_{liq}, green, and τ_{ice}, purple) and droplet effective radius (R_{liq}, orange) from MIX-CRA, shading indicates 2σ uncertainties. (b) Surface aerosol particle number concentrations (1-min mean), N_{250} (red) and N_{20} (blue). (c) Backscatter (grey shading), vertical visibility (cyan points), and obscured flag (orange) from the ceilometer. (d) Near surface temperature profile (reds) and fog liquid water path (LWP, blue, shading indicates 2σ uncertainties). (e) Upwards sensible heat fluxes at 2 m (solid) and 14 m (dashed). (f) Sodar backscatter, red dashed line indicates the height of strongest negative backscatter gradient (when Δlog(backscatter) $<$ -0.8 m^{-1}).

low winds speeds (90 % of which range from 1.65 to 3.86 m s^{-1}) throughout the event indicates that advection at the surface is unlikely to be an important process on the timescale of this event. Alternatively, this near-surface heating could result from the mixing of warm air down from above. The sensible heat fluxes at 2 m and 14 m are small (mostly < 2.5 W m^{-2}, fig. 11e) suggesting that this mixing was not driven by changes in thermodynamic stability at the surface. However, there is evidence both in the ceilometer backscatter (fig. 11c) and the sodar acoustic backscatter (fig. 11f) of features propagating downwards towards the surface. These could be remnants of mesoscale dynamical features, such as buoyancy waves, mixing warmer air down from higher in the atmosphere, or entrainment driven by radiative cooling at fog top. In either case, propagation of these features down to the surface coincide with the sudden increase in N_{20}, suggesting this is related to the mixing of more polluted air down to the surface from above into what was previously an isolated stable surface layer.

The top of the strong surface echo in the sodar backscatter, identified by the maximum negative gradient (fig. 11f), is associated with the top of the stable near-surface layer which is isolated from above by a strong surface-based temperature inversion (fig. 11d). The top of this layer decreases intermittently with height between 05:00 and 07:00, and these variations are strongly anti-correlated with N_{20} (Pearson's r = -0.69, p-value < 0.001). For example, the top of the strong sodar echo falls to 5 m a.g.l at 05:20, coinciding with the initial sharp increase in N_{20} and an increase in surface temperature. Between 05:35 and 05:55, the height of the sodar echo increases again to 8 m a.g.l and N_{20} decreases, before increasing again once the sodar echo height lowers at 05:55. This pattern continues until 06:50 after which the surface temperature inversion is completely eroded at 9 m a.g.l and the near-surface echo in the sodar disappears. The erosion of the isolated surface layer from above indicated by the sodar echo, and the anti-correlation between the surface layer height and N_{20}, is consistent with the hypothesis that the increase in N_{20} is related to the mixing of air down from above.

During the most optically thick part of the fog there was also detectable ice that increased between 05:50 and 06:10. The increase in ice optical depth coincident with a decrease in liquid optical depth could be indicative of ice growing at the expense of liquid water droplets (i.e. via the Wegener-Bergeron-Findeisen process). This would result in the evaporation of liquid droplets and the release of any aerosol particles they contain within the surface layer. In this situation, liquid droplets could form due to radiative cooling at fog top in a layer of the atmosphere where aerosol particle concentrations might be higher than at the surface, these droplets could then settle and mix towards the surface, eventually reaching a lower level that is sub-saturated with respect to water but supersaturated with respect to ice. The droplets would then evaporate, releasing aerosol particles into the surface layer. This process has been observed in Arctic mixed-phase stratocumulus clouds (Igel et al., 2017), and could also contribute to an increase in N_{20}, but it is unlikely to be the sole process driving the (~ 1000 cm^{-3}) increase in N_{20} because the typical number concentration of fog droplets at Summit is only $\sim$10 to 50 cm^{-3} (Cox et al., 2019).

When the surface temperature inversion was completely eroded above 9 m a.g.l at 06:50, the fog dissipated, and the surface began to cool again (fig. 11d). At this time, N_{250} had decreased to near-zero, suggesting that there were no further particles > 250 nm diameter available to act as CCN or INP. The cooling of the near-surface air would have increased saturation near the surface, potentially initiating the second phase of the fog. The increase in LWP during the second phase of the fog coincided with a sharp depletion of N_{20} and given that there were no particles > 250 nm left to activate, the decrease in N_{20} during the second phase of the fog was likely associated with the activation of N_{20} particles into fog droplets and the scavenging of particles by fog droplets close to the surface.

This case illustrates some of the complexities of the relationship between dynamics, thermodynamics, and aerosol properties during mixed-phase fog events, and it is not possible to say definitively what processes were involved from looking at the available observations alone. The observational evidence supports the hypothesis that the sharp increase in N_{20} associated with this fog event resulted from the mixing of higher N_{20} concentrations down to the surface, which was either driven by the fog itself (i.e. radiative cooling at fog top), or both the fog and changes in N_{20} were forced by the same external mixing event (e.g. buoyancy waves).

5.3 The impact of multiple fog events on the surface aerosol particle number concentration.

In this section we look for evidence that multiple consecutive fog events in quiescent conditions can act to deplete the near surface aerosol particle number concentration with the potential to impact fog development later in time. Fog with an observable radiative impact at the surface formed on four out of the five evenings between 01 and 06 August 2019 (fog case numbers 6 to 9, table 1), with skies otherwise clear throughout the day; associated with a persistent (weakening) high-pressure system over central Greenland (fig. S5, supporting information). Although this persistent anticyclone contributed to the unprecedented GrIS surface melt in 2019 (Tedesco & Fettweis, 2020), similar events are common over Greenland in the summer (occurring 30% of the time in JJA 1981-2010; Tedesco & Fettweis, 2020). During this event, the near-surface winds were consistently from the south-east, with 90% of measured 1-minute averaged wind speeds ranging from 1.26 to 4.81 m s^{-1}. There was a strong diurnal cycle, with radiative cooling in the near-surface layer beginning in the evening when the sun dropped below ~25° and lasting until the sun rose above ~15° the following morning (fig. 12b).

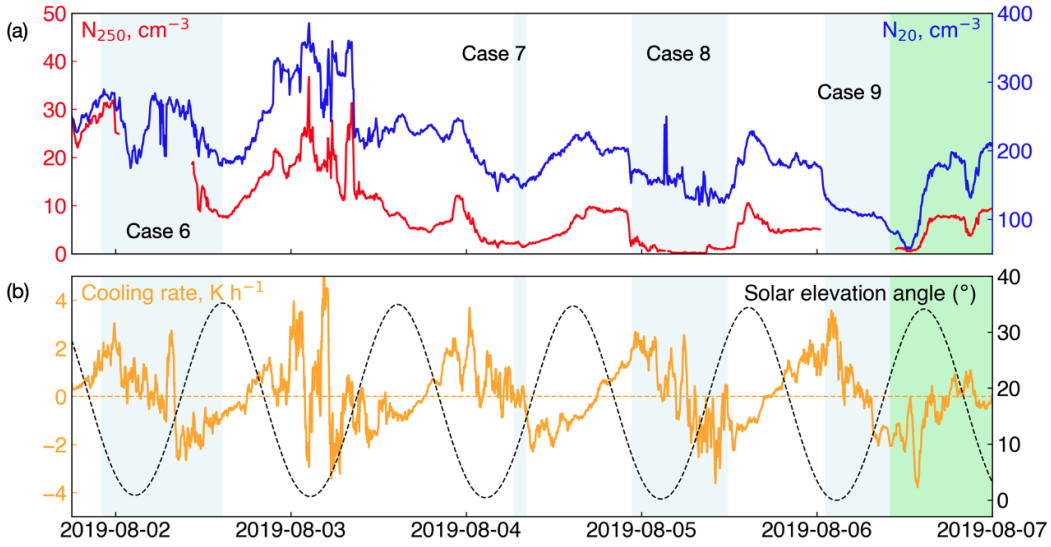

Figure 12. Surface aerosol particle number concentrations (a) and cooling rate (b) during a five day clear sky period in August 2019. Radiation fog events are highlighted in light blue, and the solar elevation angle is shown by the black dashed line on panel (b). The green highlighted region at the end of the period indicates the start of a cloudy period.

The initial N_{250} averaged over the two hours prior to case 6 was 27.7 cm^{-3}, and N_{20} was 262 cm^{-3}. Both concentrations are higher than the seasonal average, associated

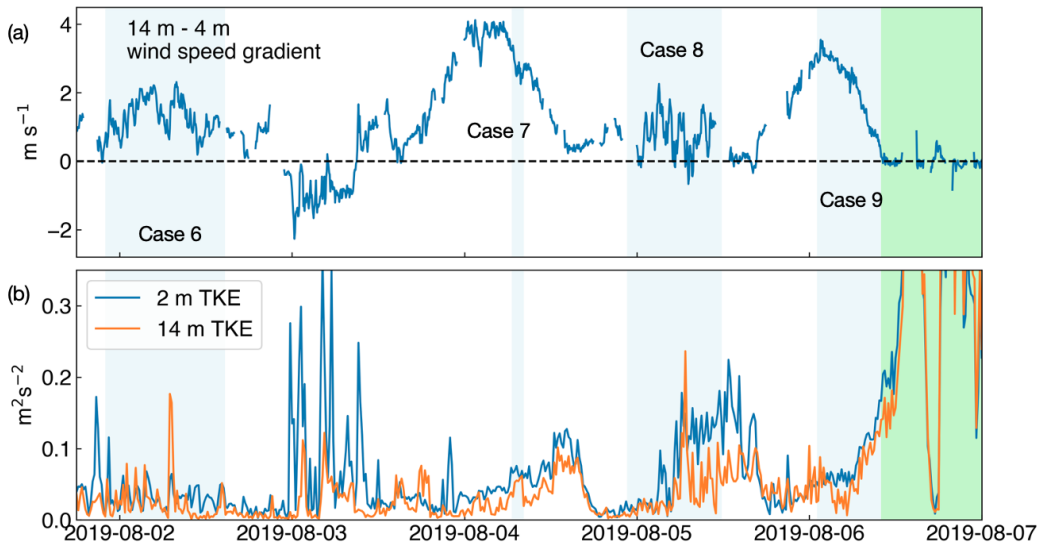

Figure 13. (a) Near surface wind shear (14 m minus 4 m wind speed, 5-minute mean) during the first week of August 2019. (b) Turbulent kinetic energy (TKE) at 2 m a.s.l (blue) and 14 m a.s.l (orange) over the same period. Radiation fog events are highlighted in blue shading as in fig. 12.

with the descent of free tropospheric air down to the surface during the high-pressure event (Guy et al., 2021). Both concentrations decrease gradually throughout the period, with daily minima generally occurring during fog events (fig. 12a). The minimum N_{250} was 0.11 cm^{-3} towards the end of case 8 (5 Aug 2019), and the minimum N_{20} was 56.5 cm^{-3}, at the end of case 9. After the end of case 9, the fog lifted from the surface, forming a low-level stratus cloud (base ∼200 m) that persisted through 7 August. Both N_{20} and N_{250} increased after the fog lifted, N_{20} to 177 cm^{-3}, and N_{250} to 7.63 cm^{-3}, but even after this recovery, both concentrations were 30% lower than the initial concentrations at the beginning of the quiescent cloud-free period.

Despite similar maximum near-surface cooling rates on the evenings with fog (2.7 to 3.7 K h^{-1}), only the first case (case 6) develops a LWP $>$ 10 g m^{-2} (fig. 6), and there is some evidence presented in section 5.1 that the development of case 8 might be limited by low aerosol particle concentration. One explanation for the gradual decrease in surface aerosol particle concentrations throughout this period (01 to 06 August) is that the scavenging of particles by fog droplets exceeds the rate of particle influx (presumably due to descent via sedimentation and/or turbulent entrainment from the free troposphere). Without measurements of vertical aerosol profiles and subsidence rates we cannot determine the relative importance of fog scavenging in this process compared to changes in particle influx (i.e. particle influx may also be decreasing with time as the anticyclonic circulation over Greenland weakens, fig. S5). However, the fact that the mean deposition flux of particles to the surface during fog events (on average 0.62 ng cm^{-2} for SO_4^{2-}, Bergin et al., 1994) is twice that of the mean dry deposition flux during the summer at Summit (0.29 ng cm^{-2} for SO_4^{2-}, Bergin et al., 1994), supports the hypothesis that multiple fog events during quiescent conditions act to deplete near surface aerosol particle concentrations, which in this case may have contributed to the latter fog cases approaching the aerosol-limited regime.

Another interesting question is why the nocturnal fog did not form on 03 August. Both near-surface temperature and aerosol concentration were highly variable early on

03 August, the maximum near-surface cooling rate reached 5.70 K h^{-1} and both N_{20} and N_{250} remained higher than the seasonal average (fig. 12), suggesting that fog formation was neither 'cooling-rate limited' nor 'aerosol limited'. Photographs from the total sky imager and observer reports of unlimited visibility confirm that the sky remained clear throughout the day. One difference between the early morning period on 03 Aug and the other mornings when fog did form is in the near-surface wind profile (fig. 13a), during the morning of 03 Aug there was a wind speed maximum close to the surface (the 4 m wind speed was consistently 1-2 m s^{-1} faster than the 14 m wind speed). The shear generated by this near-surface wind-speed jet modified the turbulent properties of the surface layer, increasing mixing (indicated by the coincident increase in turbulent kinetic energy, fig. 13b), which may have been sufficient to prevent the formation of fog droplets and likely contributed to the high variability in the near-surface aerosol concentrations and temperature profile.

6 Summary and conclusions

The first goal of this study was to highlight the advantages and limitations of using spectral ground-based measurements of downwelling longwave radiation (measured by the AERI) to examine fog microphysical properties. Unlike active remote sensing instruments, which have a blind range close to the instrument, the AERI is most sensitive to the near-surface atmosphere, making it particularly suitable for the study of shallow fogs. Measurements of shallow fog with an AERI at Summit Station, in central Greenland, also benefit from the extreme dryness of the atmosphere and the improved ability to characterize temperature and humidity near the surface. The 8-19 μm spectral range of the AERI is most sensitive to fog (or cloud) microphysical properties when the fog visible optical depth is close to 1. This is particularly advantageous for the study of optically thin clouds in polar regions (particularly fogs), which can be responsible for the maximum cloud radiative forcing at the surface during summer months (e.g. Miller et al., 2015). At Summit, optically thin fogs are common (the maximum mixed-phase optical depth retrieved from the 12 fog cases in this study is 4.8, and the mean is 0.8) so the sensitivity of the AERI instrument (which can detect LWP as low as 3 g m^{-2}) is particularly suited for the study of these fogs. However, the loss of sensitivity to fog microphysical properties at optical depths > 6 means that this technique is not appropriate for studying the microphysical properties of optically thick fogs/clouds.

The MIXCRA algorithm is designed to retrieve the optical depth of liquid droplets, the optical depth of ice crystals, and the effective radius of the liquid and ice particles from the measured spectral radiance. Although MIXCRA retrievals of cloud properties have been validated against independent measurements in multiple previous studies, this is the first validation of the MIXCRA algorithm for fog events. A cross-validation of droplet effective radius retrieved using the MIXCRA algorithm with in-situ measurements from an FM100 forward scattering probe demonstrates that MIXCRA can capture variations in R_{liq} with a RMSE of 2.0 μm when the fog optical depth is sufficient ($0.25 < \tau < 6.0$).

The loss of sensitivity of the spectral infrared signature to changes in fog microphysical properties as the fog optical depth approaches zero means that MIXCRA is unable to retrieve fog microphysical properties during the initial growth phase of fog. This also means that MIXCRA is unable to retrieve microphysical properties associated with tenuous fogs (or higher clouds) that are potentially limited by low aerosol particle number concentration. We would expect such events to be characterised by large droplet effective radius and low optical depths, but for the two potential examples shown in this study, the optical depths are too low for MIXCRA to determine the fog phase or particle effective radius.

For the 12 fog cases studied, 92% of retrievals passed the initial quality control (radiances calculated using retrieved cloud properties matched measured radiances to within

an RMSE of 1.2 RU). Where there was sufficient optical depth for the retrieval ($\tau > 0.25$), the mean total (liquid plus ice) optical depth across all fog events was 0.78 ± 0.71 (one standard deviation). Nine of the twelve cases were mixed-phase fogs, one consisted of only ice particles, one of only liquid droplets, and one case was too optically thin for any valid retrievals. The mean ice particle effective radius was 24.0 ± 7.8 μm, and the mean liquid droplet effective radius was 14.0 ± 2.8 μm. The sensitivity of the AERI allows for the detection of LWP as small as 2.0-3.0 g m^{-2} (for R_{liq} 12 to 18 μm) with a 2σ uncertainty of 0.9-1.5 g m^{-2}. The mean LWP across all fog events was 7.9 ± 6.6 g m^{-2}, and in two cases the maximum LWP exceeded 30 g m^{-2}.

The second objective of this study was to use the MIXCRA microphysical retrievals alongside measurements of surface aerosol number concentration to look for observational evidence of fog-aerosol interactions at Summit. In all cases apart from one, the concentration of aerosol particles > 250 nm (N_{250}) decreased to < 0.5 cm^{-3} during the fog event (with a median decrease of 82% after 300 minutes), suggesting that almost all particles in this size range are activated into (or scavenged by) fog droplets, consistent with past studies (Bergin et al., 1994, 1995). Changes in the concentration of 20 to 230 nm diameter particles (N_{20}) were more variable; in some cases, N_{20} was found to be well correlated with N_{250} and decreased by up to 50% during fog, whereas in others, the two populations were decoupled, and on two occasions there was a > 100% increase in N_{20} during fog.

In two case studies, there is observational evidence that the near-surface aerosol particle number concentration might be a critical control on fog LWP and lifetime, but in other cases there is evidence that dynamical processes (i.e. turbulent mixing, subsidence, or the near-surface wind profile) are more important. Large-eddy simulations based on these detailed case studies are necessary to determine why some cases developed into well-mixed optically thick fogs and others did not, which is important for the resulting net radiative forcing of the fog at the ice sheet surface. In one case study there is evidence that fog can act to increase the near-surface aerosol particle number concentration by enhancing mixing of air from above into the near-surface stable layer. During a separate period of clear skies and low winds, when nocturnal radiation fog formed on four out of five consecutive nights, a gradual reduction in N_{20} and N_{250} supports the hypothesis that multiple fog events in quiescent periods act to clean the near-surface layer of aerosol particles.

The examples presented in this study demonstrate that there are multiple pathways through which the surface aerosol population may (or may not) impact fog development, and through which fog itself can modify the surface aerosol population. Correlations between aerosol properties and fog (or cloud) microphysics should not be considered in isolation, because there are other completing processes that can impact fog development, such as the thermodynamic and turbulent structure of the boundary layer. A larger dataset of fog cases studies is necessary to investigate the competing effects of the scavenging of surface aerosol particles by fog versus increases in aerosol particles during fog events, and the importance of both processes for fog and cloud formation later in time.

Open Research Section

AERI data and the thermodynamic profiles used to drive the MIXCRA algorithm are in the process of being submitted to the Arctic Data Center at `https://doi.org/10.5439/1880028`. The temperature dependent single scattering property databases are available online at `https://people.nwra.com/rowe/refractive_indices.shtml`. The FM100 data from Cox et al. (2019) are archived at `https://doi.org/10.18739/A28K74W5W` (Noone & Cox, 2019). Aerosol particle number concentration measurements, near surface temperature and wind profiles from the 15 m tower, and sensible heat flux measure-

ments are available from CEDA data archive (Guy et al., 2020). ICECAPS ceilometer data (`https://doi.org/10.18739/A27659G3R`) and sodar data (`https://doi.org/10.18739/A2HM52K68`) are archived at the Arctic Data Center (Shupe, 2020a, 2020b). The MIXCRA retrievals used in this study are in the process of being submitted to the Arctic Data Center and are available upon request.

Acknowledgments

The efforts of technicians at Summit Station and science support provided by Polar Field Services were crucial to maintaining data quality and continuity at Summit. ICECAPS is a long-term research program with many collaborators, and we are grateful for all their efforts in developing and maintaining the various instruments and data products used in this study. Thank you also to Professor Ken S. Carslaw for proof-reading and providing valuable feedback on this publication. Financial support for ICECAPS was provided by NSFGEO-NERC grants 1801477 and 2137083. HG was funded by the NERC SPHERES DTP grant number NE/L002574/1. MDS was supported by the National Science Foundation (OPP-1801477, OPP-2137091) and the NOAA cooperative agreement (NA22OAR4320151). PMR was supported by the National Science Foundation OPP Grant 2127632. Ceilometer data were provided by the Atmospheric Radiation Measurement (ARM) User Facility, a U. S. Department of Energy (DOE) Office of Science User Facility managed by the Biological and Environmental Research Program. This work used JASMIN, the UK collaborative data analysis facility.

References

Ackerman, A. S., Kirkpatrick, M. P., Stevens, D. E., & Toon, O. B. (2004). The impact of humidity above stratiform clouds on indirect aerosol climate forcing. *Nature*, *432*(7020), 1014–1017.

Antonelli, P., Revercomb, H., Sromovsky, L., Smith, W., Knuteson, R., Tobin, D., ... Best, F. (2004). A principal component noise filter for high spectral resolution infrared measurements. *Journal of Geophysical Research: Atmospheres*, *109*(D23).

Baccarini, A., Karlsson, L., Dommen, J., Duplessis, P., Vüllers, J., Brooks, I. M., ... others (2020). Frequent new particle formation over the high arctic pack ice by enhanced iodine emissions. *Nature communications*, *11*(1), 1–11.

Bergin, M., Jaffrezo, J., Davidson, C., Caldow, R., & Dibb, J. (1994). Fluxes of chemical species to the greenland ice sheet at summit by fog and dry deposition. *Geochimica et cosmochimica acta*, *58*(15), 3207–3215.

Bergin, M., Jaffrezo, J.-L., Davidson, C., Dibb, J. E., Pandis, S., Hillamo, R., ... Makela, T. (1995). The contributions of snow, fog, and dry deposition to the summer flux of anions and cations at summit, greenland. *Journal of Geophysical Research: Atmospheres*, *100*(D8), 16275–16288.

Berkelhammer, M., Noone, D. C., Steen-Larsen, H. C., Bailey, A., Cox, C. J., O'Neill, M. S., ... White, J. W. (2016). Surface-atmosphere decoupling limits accumulation at summit, greenland. *Science Advances*, *2*(4).

Boutle, I., Angevine, W., Bao, J.-W., Bergot, T., Bhattacharya, R., Bott, A., ... others (2022). Demistify: a large-eddy simulation (les) and single-column model (scm) intercomparison of radiation fog. *Atmospheric Chemistry and Physics*, *22*(1), 319-333.

Boutle, I., Price, J., Kudzotsa, I., Kokkola, H., & Romakkaniemi, S. (2018). Aerosol–fog interaction and the transition to well-mixed radiation fog. *Atmospheric Chemistry and Physics*, *18*(11), 7827–7840.

Carslaw, K. S. (2022). Aerosol processes. In *Aerosols and climate* (pp. 135–185). Elsevier.

Clough, S. A., & Iacono, M. J. (1995). Line-by-line calculation of atmospheric fluxes

and cooling rates: 2. application to carbon dioxide, ozone, methane, nitrous oxide and the halocarbons. *Journal of Geophysical Research: Atmospheres*, *100*(D8), 16519–16535.

Clough, S. A., Iacono, M. J., & Moncet, J.-L. (1992). Line-by-line calculations of atmospheric fluxes and cooling rates: Application to water vapor. *Journal of Geophysical Research: Atmospheres*, *97*(D14), 15761–15785.

Cox, C. J., Noone, D. C., Berkelhammer, M., Shupe, M. D., Neff, W. D., Miller, N. B., ... Steffen, K. (2019). Supercooled liquid fogs over the central greenland ice sheet. *Atmospheric Chemistry and Physics*, *19*(11), 7467–7485.

Cox, C. J., Walden, V. P., Compo, G. P., Rowe, P. M., Shupe, M. D., & Steffen, K. (2014). Downwelling longwave flux over summit, greenland, 2010–2012: Analysis of surface-based observations and evaluation of era-interim using wavelets. *Journal of Geophysical Research: Atmospheres*, *119*(21), 12–317.

Cox, C. J., Walden, V. P., & Rowe, P. M. (2012). A comparison of the atmospheric conditions at eureka, canada, and barrow, alaska (2006–2008). *Journal of Geophysical Research: Atmospheres*, *117*(D12).

Creamean, J. M., Barry, K., Hill, T. C., Hume, C., DeMott, P. J., Shupe, M. D., ... others (2022). Annual cycle observations of aerosols capable of ice formation in central arctic clouds. *Nature communications*, *13*(1), 1–12.

Creamean, J. M., Kirpes, R. M., Pratt, K. A., Spada, N. J., Maahn, M., De Boer, G., ... China, S. (2018). Marine and terrestrial influences on ice nucleating particles during continuous springtime measurements in an arctic oilfield location. *Atmospheric Chemistry and Physics*, *18*(24), 18023–18042.

Field, P. R., Lawson, R. P., Brown, P. R., Lloyd, G., Westbrook, C., Moisseev, D., ... others (2017). Secondary ice production: Current state of the science and recommendations for the future. *Meteorological Monographs*, *58*, 7–1.

Gallagher, M. R., Shupe, M. D., & Miller, N. B. (2018). Impact of atmospheric circulation on temperature, clouds, and radiation at summit station, greenland, with self-organizing maps. *Journal of Climate*, *31*(21), 8895–8915.

Garrett, Fallgatter, C., Shkurko, K., & Howlett, D. (2012). Fall speed measurement and high-resolution multi-angle photography of hydrometeors in free fall. *Atmospheric Measurement Techniques*, *5*(11), 2625–2633.

Garrett, Radke, L. F., & Hobbs, P. V. (2002). Aerosol effects on cloud emissivity and surface longwave heating in the arctic. *Journal of the Atmospheric Sciences*, *59*(3), 769-778.

Garrett, & Zhao, C. (2013). Ground-based remote sensing of thin clouds in the arctic. *Atmospheric Measurement Techniques*, *6*(5), 1227–1243.

Gultepe, I., Tardif, R., Michaelides, S. C., Cermak, J., Bott, A., Bendix, J., ... others (2007). Fog research: A review of past achievements and future perspectives. *Pure and applied geophysics*, *164*(6), 1121–1159.

Gultepe, I., Zhou, B., Milbrandt, J., Bott, A., Li, Y., Heymsfield, A. J., ... others (2015). A review on ice fog measurements and modeling. *Atmospheric Research*, *151*, 2–19.

Guy, H., Brooks, I., Carslaw, K., Murray, B., Walden, V., Shupe, M., ... others (2021). Controls on surface aerosol number concentrations and aerosol-limited cloud regimes over the central greenland ice sheet. *Atmospheric Chemistry and Physics*, 1–36.

Guy, H., Neely III, R. R., & Brooks, I. (2020). ICECAPS-ACE: Integrated Characterization of Energy, Clouds, Atmospheric state, and Precipitation at Summit, Greenland - Aerosol Cloud Experiment measurements. *Centre for Environmental Data Analysis*. Retrieved from `http://catalogue.ceda.ac.uk/uuid/f06c6aa727404ca788ee3dd0515ea61a` ([Dataset] Last accessed: 23 November 2022)

Guy, H., Turner, D. D., Walden, V. P., Brooks, I. M., & Neely, R. R. (2022). Passive ground-based remote sensing of radiation fog. *Atmospheric Measurement Tech-*

niques Discussions, 1–31.

Haeffelin, M., Dupont, J.-C., Boyouk, N., Baumgardner, D., Gomes, L., Roberts, G., & Elias, T. (2013). A comparative study of radiation fog and quasi-fog formation processes during the parisfog field experiment 2007. *Pure and Applied Geophysics*, *170*(12), 2283–2303.

Hanna, E., Cappelen, J., Fettweis, X., Mernild, S. H., Mote, T. L., Mottram, R., ... Hall, R. J. (2021). Greenland surface air temperature changes from 1981 to 2019 and implications for ice-sheet melt and mass-balance change. *International Journal of Climatology*, *41*, E1336–E1352.

Hoch, S., Calanca, P., Philipona, R., & Ohmura, A. (2007). Year-round observation of longwave radiative flux divergence in greenland. *Journal of Applied Meteorology and Climatology*, *46*(9), 1469–1479.

Hofer, S., Tedstone, A. J., Fettweis, X., & Bamber, J. L. (2019). Cloud microphysics and circulation anomalies control differences in future greenland melt. *Nature Climate Change*, *9*(7), 523–528.

Howat, I., Negrete, A., & Smith, B. (2017). The greenland ice mapping project (gimp) land ice and ocean classification mask, version 1. *NASA National Snow and Ice Data Center Distributed Active Archive Center.*. doi: https://doi.org/10.5067/B8X58MQBFUPA

Igel, A. L., Ekman, A. M., Leck, C., Tjernström, M., Savre, J., & Sedlar, J. (2017). The free troposphere as a potential source of arctic boundary layer aerosol particles. *Geophysical Research Letters*, *44*(13), 7053–7060.

Kanji, Z. A., Ladino, L. A., Wex, H., Boose, Y., Burkert-Kohn, M., Cziczo, D. J., & Krämer, M. (2017). Overview of ice nucleating particles. *Meteorological Monographs*, *58*, 1–1.

Knuteson, R., Revercomb, H., Best, F., Ciganovich, N., Dedecker, R., Dirkx, T., ... others (2004a). Atmospheric emitted radiance interferometer. part ii: Instrument performance. *Journal of Atmospheric and Oceanic Technology*, *21*(12), 1777–1789.

Knuteson, R., Revercomb, H., Best, F., Ciganovich, N., Dedecker, R., Dirkx, T., ... others (2004b). Atmospheric emitted radiance interferometer. part i: Instrument design. *Journal of Atmospheric and Oceanic Technology*, *21*(12), 1763–1776.

Korolev, A. (2007). Limitations of the wegener–bergeron–findeisen mechanism in the evolution of mixed-phase clouds. *Journal of the Atmospheric Sciences*, *64*(9), 3372–3375.

Lawson, R. P., Baker, B. A., Schmitt, C. G., & Jensen, T. (2001). An overview of microphysical properties of arctic clouds observed in may and july 1998 during fire ace. *Journal of Geophysical Research: Atmospheres*, *106*(D14), 14989–15014.

Leaitch, W. R., Korolev, A., Aliabadi, A. A., Burkart, J., Willis, M. D., Abbatt, J. P., ... others (2016). Effects of 20–100 nm particles on liquid clouds in the clean summertime arctic. *Atmospheric Chemistry and Physics*, *16*(17), 11107–11124.

Lubin, D., Zhang, D., Silber, I., Scott, R. C., Kalogeras, P., Battaglia, A., ... others (2020). Aware: The atmospheric radiation measurement (arm) west antarctic radiation experiment. *Bulletin of the American Meteorological Society*, *101*(7), E1069–E1091.

Maalick, Z., Kühn, T., Korhonen, H., Kokkola, H., Laaksonen, A., & Romakkaniemi, S. (2016). Effect of aerosol concentration and absorbing aerosol on the radiation fog life cycle. *Atmospheric Environment*, *133*, 26–33.

Mahesh, A., Walden, V. P., & Warren, S. G. (2001). Ground-based infrared remote sensing of cloud properties over the antarctic plateau. part ii: Cloud optical depths and particle sizes. *Journal of Applied Meteorology and Climatology*, *40*(7), 1279–1294.

Mason, R., Si, M., Chou, C., Irish, V., Dickie, R., Elizondo, P., ... others (2016). Size-resolved measurements of ice-nucleating particles at six locations in north america and one in europe. *Atmospheric Chemistry and Physics*, *16*(3), 1637–1651.

Mattingly, K., Mote, T., & Fettweis, X. (2018). Atmospheric river impacts on greenland ice sheet surface mass balance. *Journal of Geophysical Research: Atmospheres*, *123*(16), 8538–8560.

Mauritsen, T., Sedlar, J., Tjernström, M., Leck, C., Martin, M., Shupe, M., ... others (2011). An arctic ccn-limited cloud-aerosol regime. *Atmospheric Chemistry and Physics*, *11*(1), 165–173.

Mazoyer, M., Burnet, F., & Denjean, C. (2022). Experimental study on the evolution of droplet size distribution during the fog life cycle. *Atmospheric Chemistry and Physics*, *22*(17), 11305–11321.

McFarquhar, G. M., Zhang, G., Poellot, M. R., Kok, G. L., McCoy, R., Tooman, T., ... Heymsfield, A. J. (2007). Ice properties of single-layer stratocumulus during the mixed-phase arctic cloud experiment: 1. observations. *Journal of Geophysical Research: Atmospheres*, *112*(D24).

McFiggans, G., Artaxo, P., Baltensperger, U., Coe, H., Facchini, M. C., Feingold, G., ... others (2006). The effect of physical and chemical aerosol properties on warm cloud droplet activation. *Atmospheric Chemistry and Physics*, *6*(9), 2593–2649.

Miller, N. B., Shupe, M. D., Cox, C. J., Walden, V. P., Turner, D. D., & Steffen, K. (2015). Cloud radiative forcing at summit, greenland. *Journal of Climate*, *28*(15), 6267–6280.

Münkel, C. (2006). Boundary layer and air quality monitoring with a commercial lidar ceilometer. In *Lidar technologies, techniques, and measurements for atmospheric remote sensing ii* (Vol. 6367, pp. 188–194).

Neff, W., Helmig, D., Grachev, A., & Davis, D. (2008). A study of boundary layer behavior associated with high no concentrations at the south pole using a minisodar, tethered balloon, and sonic anemometer. *Atmospheric Environment*, *42*(12), 2762–2779.

Noone, D., & Cox, C. (2019). Closing the Isotope Hydrology at Summit: Measurements of Source Regions, Precipitation and Post-deposition Processes, Greenland, 2011-2014. *Arctic Data Center*.

Pettersen, C., Henderson, S. A., Mattingly, K. S., Bennartz, R., & Breeden, M. L. (2022). The critical role of euro-atlantic blocking in promoting snowfall in central greenland. *Journal of Geophysical Research: Atmospheres*, *127*(6).

Porter, G. C., Adams, M. P., Brooks, I. M., Ickes, L., Karlsson, L., Leck, C., ... others (2022). Highly active ice-nucleating particles at the summer north pole. *Journal of Geophysical Research: Atmospheres*, *127*(6), e2021JD036059.

Price, J. (2011). Radiation fog. part i: observations of stability and drop size distributions. *Boundary-layer meteorology*, *139*(2), 167–191.

Rathke, C., Neshyba, S., Shupe, M. D., Rowe, P., & Rivers, A. (2002). Radiative and microphysical properties of arctic stratus clouds from multiangle downwelling infrared radiances. *Journal of Geophysical Research: Atmospheres*, *107*(D23), AAC–12.

Reutter, P., Su, H., Trentmann, J., Simmel, M., Rose, D., Gunthe, S., ... Pöschl, U. (2009). Aerosol-and updraft-limited regimes of cloud droplet formation: influence of particle number, size and hygroscopicity on the activation of cloud condensation nuclei (ccn). *Atmospheric Chemistry and Physics*, *9*(18), 7067–7080.

Richter, P., Palm, M., Weinzierl, C., Griesche, H., Rowe, P. M., & Notholt, J. (2022). A dataset of microphysical cloud parameters, retrieved from fourier-transform infrared (ftir) emission spectra measured in arctic summer 2017. *Earth System Science Data*, *14*(6), 2767–2784.

Rothman, L. S., Gordon, I. E., Barbe, A., Benner, D. C., Bernath, P. F., Birk, M., ... others (2009). The hitran 2008 molecular spectroscopic database. *Journal of Quantitative Spectroscopy and Radiative Transfer*, *110*(9-10), 533–572.

Rowe, Fergoda, M., & Neshyba, S. (2020). Temperature-dependent optical properties of liquid water from 240 to 298 k. *Journal of Geophysical Research: Atmospheres*, *125*(17), e2020JD032624.

Rowe, Neshyba, S., & Walden, V. (2013). Radiative consequences of low-temperature infrared refractive indices for supercooled water clouds. *Atmospheric Chemistry and Physics*, *13*(23), 11925–11933.

Rowe, Walden, V. P., Brandt, R. E., Town, M. S., Hudson, S. R., & Neshyba, S. (2022). Evaluation of temperature-dependent complex refractive indices of supercooled liquid water using downwelling radiance and in-situ cloud measurements at south pole. *Journal of Geophysical Research: Atmospheres*, *127*(1), e2021JD035182.

Schmeisser, L., Backman, J., Ogren, J. A., Andrews, E., Asmi, E., Starkweather, S., ... others (2018). Seasonality of aerosol optical properties in the arctic. *Atmospheric Chemistry and Physics*, *18*(16), 11599–11622.

Schmitt, C. G., Stuefer, M., Heymsfield, A. J., & Kim, C. K. (2013). The microphysical properties of ice fog measured in urban environments of interior alaska. *Journal of Geophysical Research: Atmospheres*, *118*(19), 11–136.

Shupe. (2020a). Ceilometer Cloud Base Height Measurements at Summit Station, Greenland, 2019. *Arctic Data Center*.

Shupe. (2020b). SOnic Detection And Ranging (SODAR) measurements taken at Summit Station, Greenland, 2019. *Arctic Data Center*.

Shupe, Turner, D. D., Walden, V. P., Bennartz, R., Cadeddu, M. P., Castellani, B. B., ... others (2013). High and dry: New observations of tropospheric and cloud properties above the greenland ice sheet. *Bulletin of the American Meteorological Society*, *94*(2), 169–186.

Shupe, Turner, D. D., Zwink, A., Thieman, M. M., Mlawer, E. J., & Shippert, T. (2015). Deriving arctic cloud microphysics at barrow, alaska: Algorithms, results, and radiative closure. *Journal of Applied Meteorology and Climatology*, *54*(7), 1675–1689.

Si, M., Irish, V. E., Mason, R. H., Vergara-Temprado, J., Hanna, S. J., Ladino, L. A., ... others (2018). Ice-nucleating ability of aerosol particles and possible sources at three coastal marine sites. *Atmospheric Chemistry and Physics*, *18*(21), 15669–15685.

Small, J. D., Chuang, P. Y., Feingold, G., & Jiang, H. (2009). Can aerosol decrease cloud lifetime? *Geophysical Research Letters*, *36*(16).

Solomon, A., Shupe, M. D., Persson, O., Morrison, H., Yamaguchi, T., Caldwell, P. M., & de Boer, G. (2014). The sensitivity of springtime arctic mixed-phase stratocumulus clouds to surface-layer and cloud-top inversion-layer moisture sources. *Journal of the Atmospheric Sciences*, *71*(2), 574–595.

Spiegel, J., Zieger, P., Bukowiecki, N., Hammer, E., Weingartner, E., & Eugster, W. (2012). Evaluating the capabilities and uncertainties of droplet measurements for the fog droplet spectrometer (fm-100). *Atmospheric Measurement Techniques*, *5*(9), 2237–2260.

Stamnes, K., Tsay, S.-C., Wiscombe, W., & Jayaweera, K. (1988). Numerically stable algorithm for discrete-ordinate-method radiative transfer in multiple scattering and emitting layered media. *Applied optics*, *27*(12), 2502–2509.

Sterzinger, L. J., Sedlar, J., Guy, H., Neely III, R. R., & Igel, A. L. (2022). Do arctic mixed-phase clouds sometimes dissipate due to insufficient aerosol? evidence from comparisons between observations and idealized simulations. *Atmospheric Chemistry and Physics*, *22*(13), 8973–8988.

Stevens, R. G., Loewe, K., Dearden, C., Dimitrelos, A., Possner, A., Eirund, G. K., ... others (2018). A model intercomparison of ccn-limited tenuous clouds in

the high arctic. *Atmospheric Chemistry and Physics*, *18*(15), 11041–11071.

Tedesco, M., & Fettweis, X. (2020). Unprecedented atmospheric conditions (1948–2019) drive the 2019 exceptional melting season over the greenland ice sheet. *The Cryosphere*, *14*(4), 1209–1223.

Turner. (2005). Arctic mixed-phase cloud properties from aeri lidar observations: Algorithm and results from sheba. *Journal of Applied Meteorology*, *44*(4), 427–444.

Turner. (2007). Improved ground-based liquid water path retrievals using a combined infrared and microwave approach. *Journal of Geophysical Research: Atmospheres*, *112*(D15).

Turner, Ackerman, S., Baum, B., Revercomb, H. E., & Yang, P. (2003). Cloud phase determination using ground-based aeri observations at sheba. *Journal of Applied Meteorology*, *42*(6), 701–715.

Turner, & Blumberg, W. G. (2019). Improvements to the aerioe thermodynamic profile retrieval algorithm. *IEEE Journal of Selected Topics in Applied Earth Observations and Remote Sensing*, *12*(5), 1339–1354.

Turner, & Eloranta, E. W. (2008). Validating mixed-phase cloud optical depth retrieved from infrared observations with high spectral resolution lidar. *IEEE Geoscience and Remote Sensing Letters*, *5*(2), 285–288.

Turner, Knuteson, R., Revercomb, H., Lo, C., & Dedecker, R. (2006). Noise reduction of atmospheric emitted radiance interferometer (aeri) observations using principal component analysis. *Journal of Atmospheric and Oceanic Technology*, *23*(9), 1223–1238.

Turner, & Löhnert, U. (2021). Ground-based temperature and humidity profiling: combining active and passive remote sensors. *Atmospheric Measurement Techniques*, *14*(4), 3033–3048.

Twomey, S. (1977). The influence of pollution on the shortwave albedo of clouds. *Journal of the atmospheric sciences*, *34*(7), 1149–1152.

Vogelmann, A. M., McFarquhar, G. M., Ogren, J. A., Turner, D. D., Comstock, J. M., Feingold, G., ... others (2012). Racoro extended-term aircraft observations of boundary layer clouds. *Bulletin of the American Meteorological Society*, *93*(6), 861–878.

Von der Weiden, S.-L., Drewnick, F., & Borrmann, S. (2009). Particle loss calculator–a new software tool for the assessment of the performance of aerosol inlet systems. *Atmospheric Measurement Techniques*, *2*(2), 479–494.

Walden, V. P., Warren, S. G., & Tuttle, E. (2003). Atmospheric ice crystals over the antarctic plateau in winter. *Journal of Applied Meteorology*, *42*(10), 1391–1405.

Williams, A. S., & Igel, A. L. (2021). Cloud top radiative cooling rate drives non-precipitating stratiform cloud responses to aerosol concentration. *Geophysical Research Letters*, *48*(18).

Yan, S., Zhu, B., Zhu, T., Shi, C., Liu, D., Kang, H., ... Lu, C. (2021). The effect of aerosols on fog lifetime: observational evidence and model simulations. *Geophysical Research Letters*, *48*(2), e2020GL61803.

Yang, P., Wei, H., Huang, H.-L., Baum, B. A., Hu, Y. X., Kattawar, G. W., ... Fu, Q. (2005). Scattering and absorption property database for nonspherical ice particles in the near-through far-infrared spectral region. *Applied optics*, *44*(26), 5512–5523.

Ziemba, L. D., Dibb, J. E., Griffin, R. J., Huey, L. G., & Beckman, P. (2010). Observations of particle growth at a remote, arctic site. *Atmospheric Environment*, *44*(13), 1649–1657.